Oncogene (2017), 1–17

www.nature.com/onc

ORIGINAL ARTICLE

EZH2 promotes neoplastic transformation through VAV interaction-dependent extranuclear mechanisms

N Venkatesan[1,8], JF Wong[1,8], KP Tan[2,3], HH Chung[1], YH Yau[1], E Cukuroglu[4], A Allahverdi[1], L Nordenskiöld[1], J Göke[4,5], S Geifman-Shochat[1], VCL Lin[1], MS Madhusudhan[2,6,7] and I-h Su[1]

Recently, we reported that the histone methyltransferase, EZH2, controls leukocyte migration through interaction with the cytoskeleton remodeling effector, VAV, and direct methylation of the cytoskeletal regulatory protein, Talin. However, it is unclear whether this extranuclear, epigenetic-independent function of EZH2 has a profound impact on the initiation of cellular transformation and metastasis. Here, we show that EZH2 increases Talin1 methylation and cleavage, thereby enhancing adhesion turnover and promoting accelerated tumorigenesis. This transforming capacity is abolished by targeted disruption of EZH2 interaction with VAV. Furthermore, our studies demonstrate that EZH2 in the cytoplasm is closely associated with cancer stem cell properties, and that overexpression of EZH2, a mutant EZH2 lacking its nuclear localization signal (EZH2ΔNLS), or a methyl-mimicking Talin1 mutant substantially promotes JAK2-dependent STAT3 activation and cellular transformation. Taken together, our results suggest a critical role for the VAV interaction-dependent, extranuclear action of EZH2 in neoplastic transformation.

Oncogene advance online publication, 2 October 2017; doi:10.1038/onc.2017.309

INTRODUCTION

EZH2 overexpression or mutation is known to associate with several aggressive human solid tumor types, including prostate cancer, breast cancer and different types of lymphomas, and is indicative of a poor prognosis in patients.[1–3] The oncogenic effect of EZH2 can be achieved through histone 3 lysine 27 trimethylation (H3K27Me3)-mediated transcriptional repression of tumor suppressor genes such as CDH1 (E-cadherin), RKIP, RAD51, DAB2IP, RUNX3 and CDKN1c ($p57^{KIP2}$).[4–7] EZH2 can also regulate gene expression indirectly through the recruitment of DNA methyltransferases to target gene promoter regions.[8] H3K27 methylation-independent roles of EZH2 have also been identified. EZH2 interactions with NF-κB in breast cancer cells promote NF-κB target gene expression[9] and EZH2 recruitment to the *NOTCH1* promoter increases NOTCH1 expression and signaling.[10] While EZH2 acts as a coactivator for the androgen receptor[11] transcription factor, it can also enhance STAT3 activity or stabilize β-catenin through the methylation of these proteins.[12,13] Furthermore, EZH2-mediated methylation of the transcription factors GATA4 and RORα results in the attenuation of their transcriptional activities.[14,15] Interestingly, the oncogenic property of EZH2 has been challenged by several recent findings that suggest a tumor suppressor role for EZH2 in T-acute lymphoblastic leukemia.[16–18] Despite intensive efforts to determine the molecular mechanisms of dysregulated EZH2 expression in oncogenesis, we still do not fully understand the role of EZH2 in this context. Therefore, the underlying mechanisms linking dysregulated EZH2 expression with cancer initiation and progression may vary depending on the cellular context and oncogenic pathways that are activated in different cancers.

Functionally, EZH2 overexpression results in the downregulation of adhesion molecules, cell cycle regulators, transcription factors and DNA repair machinery,[4–7,19,20] and these changes have been shown to contribute to cellular transformation and metastasis. Furthermore, our previous study identified a cytosolic EZH2 complex associated with another group of proto-oncogenes, the VAV family of proteins.[21–23] VAV proteins are guanine nucleotide exchange factors (GEFs) for Rho family GTPases that are involved in cell adhesion, migration and proliferation of normal cells as well as the pathogenesis of cancer cells.[24–28] More specifically, VAV2/VAV3 are shown to be essential for the development of breast cancer and skin tumors,[28,29] while VAV2 is suggested to be recruited to epidermal growth factor receptor (EGFR) during the morphological transformation of mammary epithelial cells.[30] In addition, VAV1 gene mutations have been detected in various human tumors[24,25,27] and an oncogenic form of VAV1, which is N-terminally truncated and does not assume an auto-inhibitory conformation,[31,32] has been shown to promote the transformation of fibroblasts.[33]

Even though there is a large amount of data showing the critical roles of EZH2 and VAV family proteins in tumorigenesis, it is not clear whether there is a functional link between EZH2 and VAVs in this context. Here, we identify the residues on EZH2 that are critical for its interaction with VAV and demonstrate that EZH2 interactions with VAV proteins are crucial for the regulation of adhesion dynamics and cellular transformation. Mechanistically, overexpression of wild-type EZH2 or EZH2 lacking its nuclear localization signal (EZH2ΔNLS) promotes Talin methylation and cleavage, thereby destabilizing adhesion structures in a VAV interaction-dependent manner. In addition, the expression of a methyl-mimicking Talin1 mutant or EZH2ΔNLS substantially enhances JAK2-dependent STAT3 activity and the expression of

---

[1] School of Biological Sciences, College of Science, Nanyang Technological University, Republic of Singapore; [2] Bioinformatics Institute, Agency for Science, Technology and Research, Biopolis, Republic of Singapore; [3] School of Computer Engineering, Nanyang Technological University, Republic of Singapore; [4] Genome Institute of Singapore, Agency for Science, Technology and Research, Biopolis, Republic of Singapore; [5] National Cancer Centre Singapore, Republic of Singapore; [6] Indian Institute of Science Education and Research, Pune, India and [7] Department of Biological Sciences, National University of Singapore, Republic of Singapore. Correspondence: Dr I-h Su, School of Biological Sciences, College of Science, Nanyang Technological University, 60 Nanyang Drive, Singapore 637551, Singapore.
E-mail: ihsu@ntu.edu.sg

[8] These two authors contributed equally to this work.

Received 22 November 2016; revised 10 July 2017; accepted 11 July 2017

STAT3 target genes associated with tumorigenesis. Taken together, our data suggest that EZH2 interactions with VAV family proteins in the cytoplasm contribute to initial neoplastic transformation and possibly the maintenance of cancer stem cells through the regulation of adhesion dynamics and STAT3 signaling pathways, which precedes the well-established functions of EZH2 in epigenetic silencing of tumor suppressors.

RESULTS

Characterization and structural prediction of the EZH2–VAV1 interaction domains

The structural details of the EZH2–VAV interaction are required for determining whether it is critical for neoplastic transformation as well as for designing a treatment strategy to interrupt the interaction. With this in mind, we narrowed down the minimal

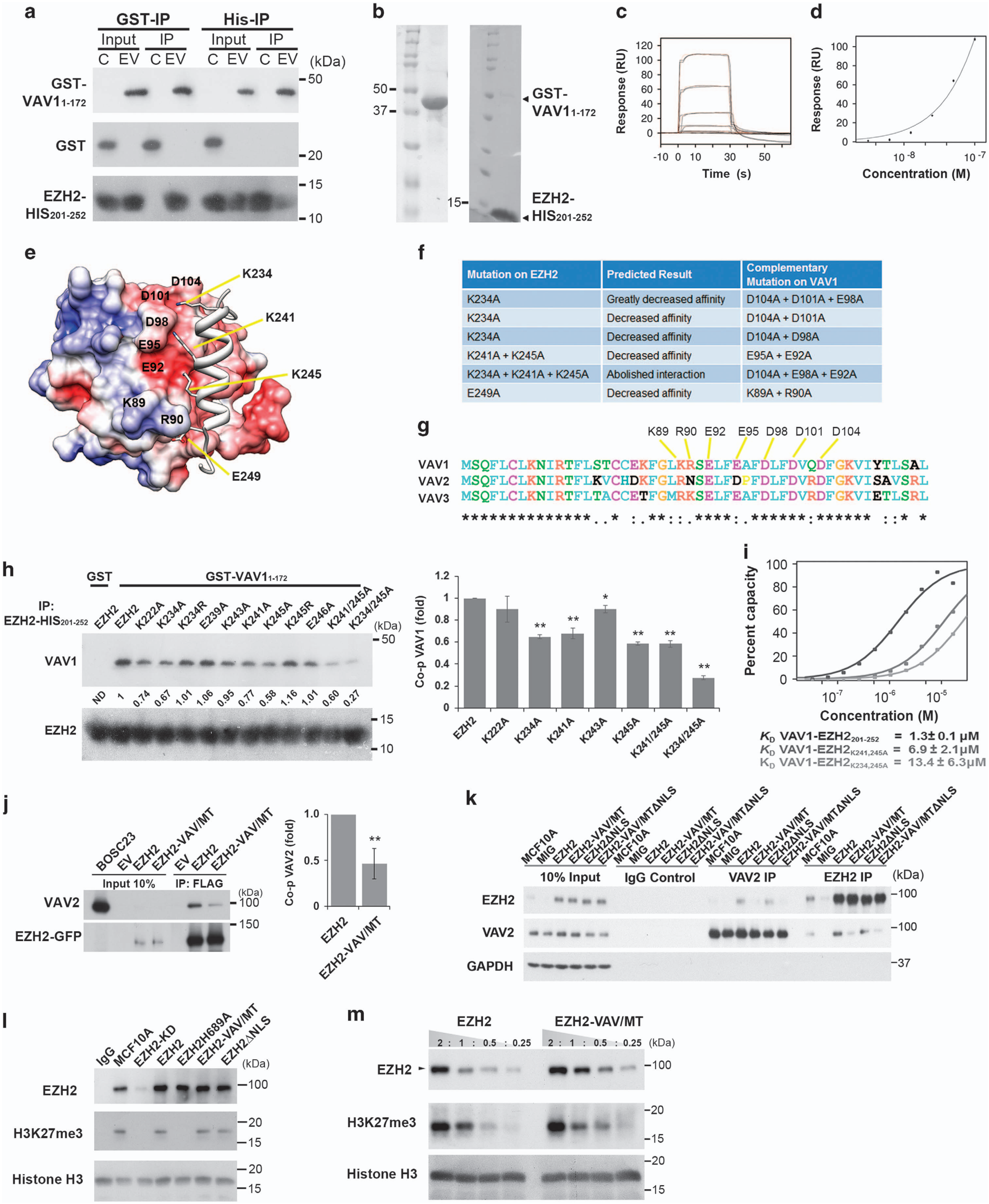

Mutation on EZH2	Predicted Result	Complementary Mutation on VAV1
K234A	Greatly decreased affinity	D104A + D101A + E98A
K234A	Decreased affinity	D104A + D101A
K234A	Decreased affinity	D104A + D98A
K241A + K245A	Decreased affinity	E95A + E92A
K234A + K241A + K245A	Abolished interaction	D104A + E98A + E92A
E249A	Decreased affinity	K89A + R90A

VAV1 interaction domain to $EZH2_{201-252}$ and confirmed the direct interaction of EZH2–VAV in the absence of other complex proteins by reciprocal pull-down experiments using recombinant EZH2 ($EZH2_{201-252}$) and VAV1 ($VAV1_{1-172}$)[21,34] fragments (Figure 1a). The binding affinity of the EZH2 and VAV1 fragments (Figure 1b) was further determined using the surface plasmon resonance-based biosensor, BIACORE, to be between 0.6 and 1.5 μM with a stoichiometry of 1:1 (Figures 1c and d). This interaction is characterized as a quick interaction with a binding affinity similar to other important biological interactions.[35]

In order to better understand the EZH2–VAV interaction on a molecular level, we attempted to co-crystallize the interaction domains of these two proteins. Unfortunately, all of our crystallization attempts failed, so we decided to employ a bioinformatics approach as an alternative to determine the critical amino-acid residues required for this interaction. Since the minimal EZH2-interacting domain of VAV1 (amino acids 66–115, reported in ref. 21,34) contains a calponin homology (CH) domain, we examined all eight known protein–protein interactions involving CH domains and observed that they all interact with helices. This pattern of CH domain interaction with helices was consistent even when the sequences of interacting helices were only weakly similar to one another (for details, see Supplementary Methods). Furthermore, electrostatic profiling of the VAV1 CH domain shows a charged interaction surface (Figure 1e), where one part of the surface is positively charged and the other end is negatively charged. On the basis of these analyses, we propose that the part of EZH2 interacting with VAV1 must be helical and that the interaction is likely to be predominated by electrostatic interactions, which is a conserved feature of all observed interactions involving CH domains.

On EZH2, two helices are predicted between residues 221–230 and residues 237–250 (Supplementary Figure 1a). Interestingly, a similar structure has been reported recently in EZH2's yeast counterpart, despite very low sequence homology between the yeast and mammalian EZH2 proteins.[36] Our analyses indicate that charge complementarity between VAV1 and EZH2 is best achieved with the second helix and thus the interaction models were fine tuned to maximize the charge complementarity. The detailed structural analysis is shown in the Supplementary Methods.

Identification of the critical residues required for EZH2–VAV1 interaction

Following our structural analyses, we generated a model of the VAV1–EZH2 complex (Figure 1e), proposing that the positively charged amino-acid residues of the EZH2 helix (K234, K241 and K245) complement the negatively charged amino-acid residues of VAV1 (E92, E95, D98, D101 and D104) (Figure 1f and Supplementary Methods). The proposed EZH2 interaction region is highly conserved between VAV1, VAV2 and VAV3 from various species (Figure 1g and Supplementary Figure 1b), suggesting that the EZH2–VAV interaction is likely to be conserved among different cell types and species. Consistent with this notion, EZH2 was shown to interact with VAV2 in non-hematopoietic lineage cells such as BOSC23, MCF10A cells and a human breast cancer cell line (Supplementary Figure 2a).

To validate our predictions, the proposed mutations were introduced into the recombinant $EZH2_{201-252}$ fragment and the resulting mutants were then tested for their abilities to interact with the wild-type VAV1 fragment using pull-down assays, as described in Figure 1a. Our data revealed that alanine substitution of lysine residues K234, K241 and K245 on EZH2 resulted in a modest, but consistent, reduction of EZH2–VAV1 interaction (Figure 1h). Subsequently, we generated the double lysine mutants EZH2-K241/K245A (reported in ref. 37) and EZH2-K234/K245A, which exhibited significant decreases in VAV1 interaction in our *in vitro* assays (Figure 1h). Using surface plasmon resonance analysis, these EZH2 mutants were shown to bind to VAV1 fragments with 5–10-fold reduced affinities (Figure 1i). Since EZH2-K234/K245A exhibited more reductions in VAV1 interaction in our assays, we utilized the EZH2-K234/K245A mutant in our

◀

Figure 1. Structural prediction and identification of the critical residues on EZH2 for EZH2–VAV interaction. (**a**) Purified GST-tagged $VAV1_{1-172}$ and 6 × His-tagged $EZH2_{201-252}$ were immunoprecipitated with either His-Pur Cobalt resin or glutathione beads. Immunoblots with the indicated antibodies are shown. 'C' indicates GST control incubated with EZH2 fragment and 'EV' indicates EZH2 fragment incubated with VAV1 fragment. (**b**–**d**) EZH2–VAV1 interaction was characterized by surface plasmon resonance (SPR) analysis. (**b**) Purified EZH2–$HIS_{201-252}$ and GST–$VAV1_{1-172}$ were analyzed by Coomassie-stained gel before being subjected to SPR analysis. (**c**) $VAV1_{1-172}$ interactions with $EZH2_{201-252}$ as determined by SPR. Sensograms obtained were buffer and reference flow cell corrected. (**d**) Equilibrium responses were plotted against the log of EZH2–$HIS_{201-252}$ concentration. The estimated affinity constant of the interaction between EZH2–$HIS_{201-252}$ and GST–$VAV1_{1-172}$ was 600 nM based on the steady-state model. (**e**) Comparative model of the VAV1–EZH2 interaction. VAV1 is shown in surface representation, while the interacting helix of EZH2 is shown as ribbon. The surface is colored by its electrostatic potential. Positive and negative regions are shaded blue and red, respectively. Detailed information for the structural analysis is listed in the Supplementary Methods. (**f**) Predicted mutations in EZH2 and the complementary mutations in VAV1 to disrupt EZH2–VAV1 interaction. (**g**) Sequence alignment of the EZH2–interacting stretch of human VAV1, VAV2 and VAV3. Alignment positions marked with an '*' indicate sequence conservation, while ':' and '.' denote levels of sequence similarity (details see Supplementary Figure 1b). (**h**) The interactions of HIS-tagged $EZH2_{201-252}$ point mutants with wild-type $VAV1_{1-172}$ fragment were determined by immobilizing EZH2 using His-Pur Cobalt resin and incubating with purified VAV1 fragments. Bar graph on the right summarizes the fold changes in VAV1 co-precipitated by EZH2 mutants relative to the amount pulled down by wild-type EZH2 from three independent experiments. Means ± s.d. are shown. $^{**}P = 0.001$, 0.007, 0.0004, 0.002, 0.0002 (left to right), $^{*}P = 0.03$ (two-tailed Student's *t*-test). (**i**) $VAV1_{1-172}$ interactions with $EZH2_{201-252}$ mutants as determined by SPR. Interactions were performed as in **c**. (**j**) Empty vector (EV), wild-type EZH2 and EZH2–VAV/MT fused with C-terminal GFP-FLAG-tags were transiently expressed in BOSC23 cells and EZH2 fusion proteins were purified using anti-FLAG antibody under stringent conditions free of interacting proteins (see input controls). The amounts of purified EZH2 variants were adjusted and incubated with BOSC23 lysates to interact with VAV2. The co-precipitated VAV2 was determined by specific antibody. Bar graph summarizes the fold changes in VAV2 (co-p VAV2) co-precipitated by EZH2–VAV/MT relative to that pulled down by wild-type EZH2 from three independent experiments. Mean ± s.d. for each condition is shown. $^{**}P = 0.005$ (two-tailed Student's *t*-test). (**k**) Whole-cell extracts of wild-type (MCF10A) or endogenous EZH2 knockdown MCF10A cells transduced with control virus (MIG) or retrovirus to express the indicated EZH2 variants were subjected to EZH2 or VAV2 immunoprecipitation. Data shown are representative of two independent experiments. (**l**) EZH2 was immunoprecipitated from total cell extracts of EZH2 knockdown MCF10A cells reconstituted with the indicated EZH2 variants and used in an *in vitro* methyltransferase assay with cold *S*-adenosyl methionine (SAM) as a methyl donor and recombinant histone octamer as a substrate. H3K27me3 was determined by immunoblot with specific antibody. (**m**) Histone methyltransferase activities of wild-type EZH2 and the VAV targeting mutant EZH2–K234/245A (EZH2–VAV/MT) immunoprecipitated from reconstituted EZH2 knockdown MCF10A cells were measured as in **l**, except with titrated amounts of EZH2, as indicated. Immunoblots shown in this figure are representative of more than three independent experiments.

subsequent studies (hereafter referred to as EZH2–VAV/MT). The reduced interaction of mutated EZH2 and VAV1 was further verified using full-length proteins (Supplementary Figure 2b) and the additional K241A mutation did not further reduce the interaction (Supplementary Figure 2c). Similarly, complementary mutations in full-length VAV1 (E92A, E98A and D104A) also led to substantial reductions in their interactions with EZH2 (Supplementary Figure 2d). Moreover, we confirmed that the interaction of EZH2–VAV/MT with VAV2, the major VAV family protein in non-hematopoietic lineage cells, was also significantly reduced both *in vitro* (Figure 1j) and in cells (Figure 1k). However, these lysine mutations on EZH2 did not disrupt interactions with components of the PRC2 core complex (SUZ12 and EED) (Supplementary Figure 2e) or compromise EZH2's histone methyltransferase (HMTase) activity*in vitro* (Figures 1l and m).

VAV interaction is required for EZH2-promoted tumorigenesis

We next sought to determine whether the interaction of EZH2 with VAV family proteins is essential for the transforming capacity of EZH2. For our initial *in vitro* assessment of transforming capacity, we overexpressed wild-type EZH2, an enzymatically inactive form of EZH2 (EZH2H689A), or the EZH2–VAV/MT mutant in the mammary epithelial cell line H16N2 and tested whether they could initiate malignant transformation using anchorage-independent cell growth assays. To enhance the EZH2 interaction with VAV in the cytosol, we also expressed a mutant EZH2ΔNLS. To avoid interference, endogenous expression of EZH2 in H16N2 cells was knocked down by lentivirus-mediated short hairpin RNA (shRNA) and the target site of the shRNA was mutated in the exogenous EZH2 constructs (Supplementary Figure 3a). The total amounts of exogenous EZH2 variants were about 4–5-fold higher than those observed in normal epithelial cells, but were physiological and comparable to the endogenous EZH2 expression levels in 4T1 and MDA-MB-231 breast cancer cells (Supplementary Figure 3a). The results of our anchorage-independent cell growth assays showed that the expression of wild-type EZH2 promoted colony formation (Figure 2a), which is consistent with previous studies.[1,5] Furthermore, we found that expression of the EZH2ΔNLS mutant resulted in a two-fold increase in cytosolic EZH2 expression levels (Supplementary Figure 3b), drastically elevated the number of breast cancer stem-like cells (Supplementary Figure 3c), and significantly promoted cellular transformation relative to results obtained for wild-type EZH2 (Figure 2a, left and middle panels). In contrast, expression of the enzymatically inactive EZH2H689A mutant or control construct (MIG) did not promote anchorage-independent cell growth (Figure 2a). Moreover, VAV2 knockdown drastically reduced the transforming capacity of EZH2ΔNLS (Figure 2a, right panel, and Supplementary Figure 3d). Similarly, expression of either the EZH2–VAV/MT mutant or an EZH2–VAV/MT mutant lacking its NLS resulted in the complete loss of EZH2-promoted cellular transformation (Figure 2a).

To determine whether VAV interaction is crucial for EZH2-promoted primary tumor growth *in vivo*, we first utilized a xenograft model of SCID mice transplanted with human breast cancer cells. For our experiments, EZH2 variants were transduced into MDA-MB-231 cells and the resulting cells were inoculated into the mammary fat pads of female NOD-SCID mice (expression of EZH2 variants is shown in Supplementary Figure 3e). Even though the percentage of exogenous EZH2 in these cells only ranged from 30 to 45% (Supplementary Figure 3e), we still observed distinct influences of EZH2 variants on tumor growth *in vivo*. The tumor growth in mice that received wild-type EZH2- or EZH2ΔNLS-expressing cells was significantly higher than the growth observed in mice that received cells expressing MIG, EZH2H689A or EZH2–VAV/MT (Figures 2b and c). Mice that received cells expressing wild-type EZH2 or EZH2ΔNLS also showed enlarged lymph nodes, which is indicative of lymph node metastasis (Figure 2d and Supplementary Figure 3f showing the presence of human origin cancer cells in lymph nodes).

To further validate the oncogenic capacity of EZH2 variants *in vivo* in a different experimental setting, we utilized the 4T1 mouse breast cancer model. Endogenous EZH2 in 4T1 cells was first lowered by specific shRNA-mediated knockdown before the cells were transduced with EZH2 mutants and inoculated into the mammary fat pads of BALB/c mice (the expression of EZH2 variants is shown in Supplementary Figure 3g). In these experiments, the exogenous EZH2 consisted of 40–65% of the total EZH2 (Supplementary Figure 3g, right panel). It was not possible to drastically increase the expression of exogenous EZH2 in cancer cells, likely due to the high level of endogenous EZH2 or potentially oncogene toxicity.[38] Our results showed that even under immune-competent conditions, EZH2 and EZH2ΔNLS were still able to greatly enhance tumor growth (Figures 2e–g). Interestingly, when we reduced the VAV-targeting capacity of the EZH2 lacking its NLS (EZH2–VAV/MTΔNLS), the elevated tumor growth and metastasis were reduced, demonstrating the critical role of the EZH2–VAV interaction in EZH2-promoted tumorigenesis (Figures 2e–g).

EZH2 promotes VAV interaction-dependent adhesion turnover

Previous work from our lab has shown that extra-nuclear EZH2 has important roles in regulating receptor-induced actin polymerization and integrin-dependent transendothelial migration in a number of different cell types.[22,37] Since malignant transformation is frequently associated with changes in the adhesive and migratory behavior of cells, we hypothesized that in addition to the epigenetic regulation of gene expression, EZH2 also controls adhesion dynamics and thereby contributes to tumorigenesis in a VAV-dependent manner. To test our hypothesis, we first investigated the formation of adhesion structures in H16N2 cells expressing EZH2 variants. While the adhesion assembly rates were comparable between cells expressing EZH2 variants, the expression of wild-type EZH2 or EZH2 lacking its NLS substantially reduced the size (Figures 3a and b, top panel) and number (Figures 3a and b, bottom panel) of adhesion structures by promoting adhesion disassembly (Figure 3c, Supplementary Video 1). Correspondingly, the areas occupied by these cells were significantly reduced (Figure 3d). In contrast, the expression of inactive EZH2 (EZH2H689A) or VAV interaction mutant EZH2 (EZH2–VAV/MT) in H16N2 cells significantly promoted the formation of large, stable, adhesion structures, such as focal and fibrillar adhesions, with very slow disassembly rates (Figures 3a–c and Supplementary Video 2), resulting in cells that spread out extensively (Figure 3d). Similarly, even in cells expressing hyperactive EZH2 (EZH2Y641F), when the interaction with VAV was disrupted, the reduction in cell spreading area was abolished, (Figure 3d, EZH2–VAV/MT-Y641F). Overall, these results are well correlated with the oncogenic capacity of the EZH2 variants shown earlier and suggest that EZH2 promotes cellular transformation at least partly through the regulation of adhesion dynamics.

EZH2-mediated Talin1 methylation regulates EGF-independent adhesion dynamics

Since VAV2 is known to be recruited to EGFR[30] and more than 30% of all breast cancers are linked to overexpression of EGFR or abnormal EGFR signaling,[39] we sought to determine whether EGF-induced disassembly of adhesions is affected by the expression of EZH2 variants. For these experiments, the aforementioned EZH2 knockdown H16N2 cells expressing EZH2 variants were EGF starved for 3 days and then re-stimulated with EGF. This treatment significantly promoted the disassembly of adhesion structures in EZH2 knockdown cells and cells expressing wild-type or cytosolic

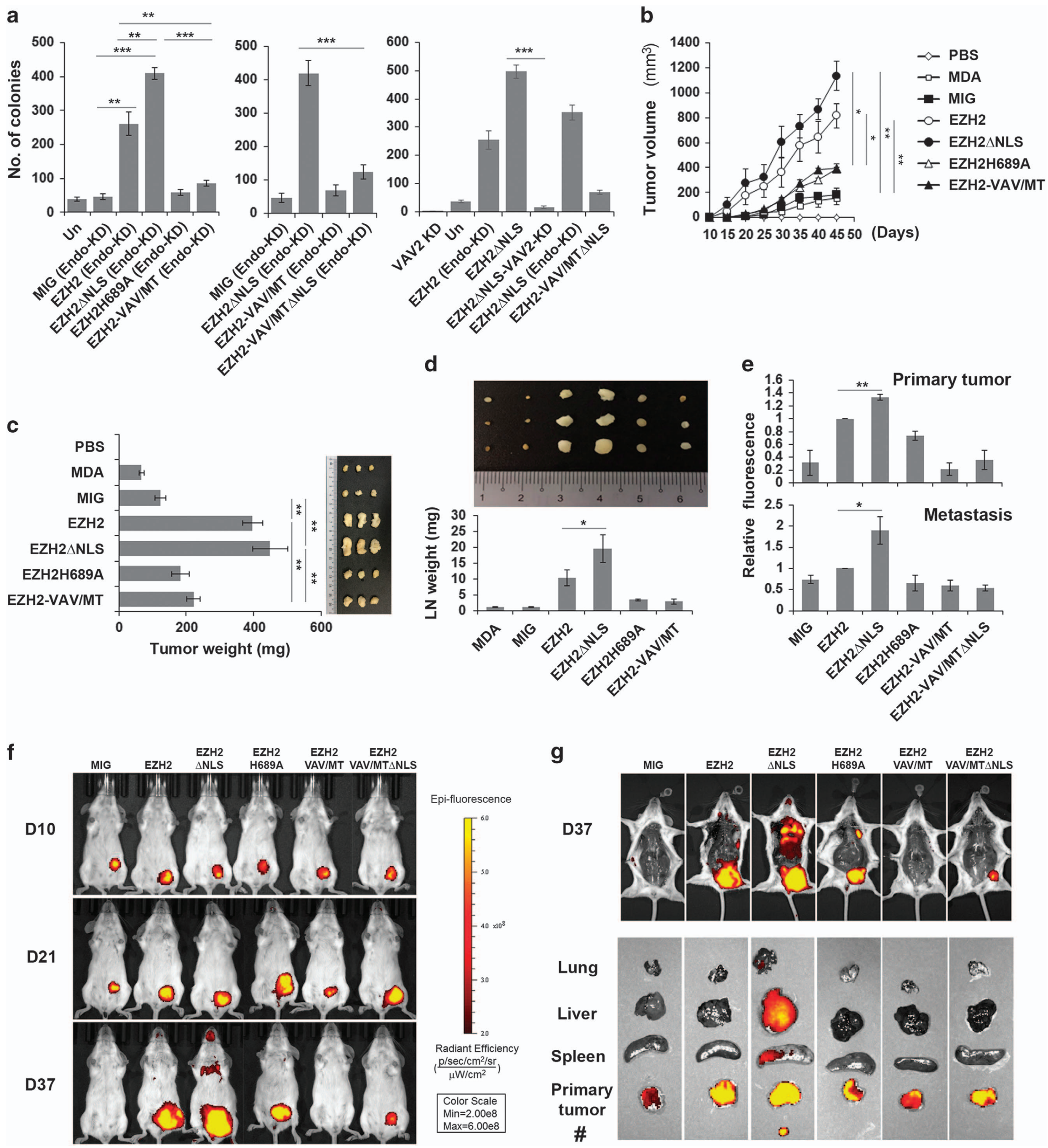

Figure 2. VAV interaction-dependent oncogenic capacity of EZH2. (**a**) Wild-type un-transduced (Un), endogenous EZH2 knockdown (Endo-KD), VAV2 knockdown (VAV2-KD) or H16N2 cells transduced with control (MIG) or retrovirus to express the indicated EZH2 variants were tested for anchorage-independent cell growth. Data represent means ± s.d., (three independent experiments with technical triplicates). Two-tailed Student's *t*-test with equal variance, left graph: $^{**}P=0.0005$, 0.002, 0.001, $^{***}P=4.8\times10^{-6}$, 8.5×10^{-6} (left to right). Middle graph: $^{***}P=1.2\times10^{-5}$. Right graph: $^{***}P=2\times10^{-13}$. (**b**–**d**) MDA-MB-231 (MDA) human breast cancer cells transduced with EZH2 variants were inoculated into the mammary fat pads of 6-week-old female NOD-SCID mice. (**b**) The tumor volumes at different time points were estimated based on the width and length measurements using a Vernier caliper, as described in Materials and methods section. Statistical analyses were performed between wild-type EZH2 or EZH2ΔNLS and EZH2–VAV/MT or MIG controls. (**c**) Tumor weight was measured at the end of experiment after killing the animal. Representative images of resected primary tumors (**c**, right panel) and draining lymph nodes (**d**, top panel) are shown. Data represent means ± s.e.m. One-tailed Student's *t*-test with equal variance, $^{*}P=0.02$, 0.04, $^{**}P=0.002$, 0.002, left to right in **b**, $^{**}P=0.0003$, 0.0002, 0.006, 0.002, top to bottom in **c**, $^{*}P=0.02$ in **d**. $n=6$ mice per group for experiments shown in **b**–**d**. (**e**–**g**) Mouse 4T1 breast tumor cells, in which endogenous EZH2 was knocked down and subsequently transduced with retrovirus for the expression of wild-type EZH2 or the indicated EZH2 variants, were inoculated into the mammary fat pads of 6-week-old female BALB/c mice. Tumor growth was monitored by manual measurement and visualized by IVIS Spectrum CT using 2-DG probe on the days indicated. (**e**) Relative 2-DG fluorescence signals of the primary tumors and metastases in the thoracic region of the animals at 37 days after inoculation are shown in bar graphs. Data represent means ± s.e.m. Two-tailed Student's *t*-test with equal variance, $^{**}P=0.002$, $^{*}P=0.048$. (**f**) Representative images of fluorescence-labeled tumors in live animals at the indicated time points are shown. (**g**) At day 37, mice were killed and the internal organs were imaged. Top and bottom panels represent data from two independent sets of experiments. The modest tumor growth enhancing effect of EZH2H689A in **f** and **g** could be due to residual enzymatic activity (20–30%) combined with high expression levels. '#' indicates neck lymph node metastases found in all mice that received EZH2ΔNLS expressing 4T1 cells. Representative images from one of two independent experiments are shown. $n=6$ animals per group for experiments shown in **e**–**g**.

EZH2 (Supplementary Figure 4). However, the prominent adhesion structures in cells expressing inactive or VAV-targeting mutant EZH2 were less sensitive to EGF-induced disassembly (Supplementary Figure 4). Moreover, EGFR signaling events, such as activation of EGFR, AKT, FAK, ERK, and the VAV downstream effector PAK1 (Supplementary Figures 5a, b), as well as recruitment of VAV2 to EGFR, VAV2 phosphorylation and EGFR degradation[30] (Supplementary Figures 5c–e) were not altered in EZH2 variants expressing mammary epithelial cells. These data suggest that even though the expression of EZH2 reduced the formation of prominent adhesion structures, EGF-induced disassembly of focal complexes/adhesions and receptor proximal signaling are likely to be independent of EZH2.

Interestingly, we repeatedly observed an increased abundance of cleaved Talin1 rod and head domains in cells expressing wild-type EZH2 or EZH2ΔNLS, but not in cells expressing inactive or VAV interaction mutant EZH2 (Figure 4a). Similar results for EZH2-promoted Talin1 cleavage were observed in BOSC23 cells expressing EZH2 variants (Figure 4b). Since our recent study in innate leukocytes revealed that EZH2-mediated methylation of Talin1 at lysine residue 2454 regulates cell migration[37] and similar EZH2-promoted Talin1 methylation (Figure 4c), and EZH2–VAV–Talin1 complexes (Figure 4d) were also observed in mammary epithelium and breast cancer cells, we hypothesized that EZH2-mediated Talin1 methylation first interferes with F-actin binding, then promotes Talin1 cleavage and subsequent disassembly of adhesion structures. Indeed, when we expressed a mutant Talin1 in which the EZH2-methylated Lys2454 was mutated to an un-methylatable alanine residue or an un-methylatable, polar glutamine residue, the binding to F-actin remained the same (K2454A, Figure 4e, left) or was increased (K2454Q, Figure 4e, right) and cleavage of these Talin1 mutants in cells was reduced (Figure 4f). Conversely, the replacement of Talin1–Lys2454 with a tri-methyl-mimicking phenylalanine residue[40] (K2454F) resulted in decreased F-actin binding (Figure 4e) and enhanced cleavage (Figure 4f). Moreover, EZH2-promoted Talin cleavage was dependent on the presence of VAV2 (Figure 4g). The effects of EZH2-mediated Talin1–K2454 methylation on adhesion structures were further confirmed in H16N2 cells expressing the Talin1–K2454 mutants described above. The expression of Talin1–K2454A or –K2454Q in H16N2 cells promoted the formation of stable focal and fibrillar adhesions (Figure 4h and Supplementary Figure 5f) with extremely slow disassembly rates (Figure 4i and Supplementary Video 3), whereas expression of Talin1–K2454F resulted in rapid disassembly of adhesions (Figure 4i and Supplementary Video 4) and increased numbers of H16N2 cells without visible adhesion structures (Supplementary Figure 5g). These results suggest that EZH2-mediated Talin1 methylation promotes Talin1 cleavage and subsequently leads to disassembly of adhesion structures.

EZH2 lacking its NLS modulates gene expression profiles favoring tumorigenesis

In order to evaluate the effects of EZH2 mutation on nuclear histone methylation, we examined the overall H3K27 trimethylation (H3K27me3) levels in H16N2 cells expressing EZH2 variants. As expected, the H3K27me3 levels in cells expressing wild-type-EZH2 or VAV interaction mutant EZH2 were comparable (Figure 5a), confirming the unaltered histone methylation capacity of the VAV targeting mutant EZH2 compared to that of wild-type EZH2, as shown earlier (Figures 1k and l). In contrast, the H3K27me3 level was reduced in cells expressing EZH2H689A reflecting the reduced enzymatic activity (Figure 5a). Even though we showed that deletion of the nuclear localization signal in EZH2 does not affect the interaction of EZH2 with PRC2 core components, EZH2's *in vitro* HMTase activity (Figure 5b, Supplementary Figure 6, Figure 1k), or the capacity of EZH2 to methylate cytosolic Talin1 in cells (Figure 4c), we found that overexpressed EZH2ΔNLS in the nucleus (Supplementary Figure 3b) contributes little to H3K27 methylation (Figure 5a). This is due to the disrupted interaction of EZH2ΔNLS and CDYL (Figure 5c, top), a co-factor that is required for chromatin targeting and efficient H3K27 methylation in cells.[41] Consequently, the recruitment of EZH2ΔNLS to EZH2 target genes, such as *ATF3* or *KDR*, was reduced (Figure 5c, middle and bottom panels). The increased EZH2 levels in the cytosol may have also sequestered other components of the PRC2 complex in the cytoplasm and reduced the histone methyltransferase capacity in the nucleus. However, the distributions of other members of the PRC2 complex, including SUZ12, EED and HDAC1, in the nucleus were not affected by the expression of any exogenous EZH2 variants (Figure 5d), but reduced SUZ12 and EED protein levels in EZH2 knockdown cells was observed, as reported previously.[42,43]

Interestingly, the expressions of several well-established transcriptional target genes of EZH2 in cancer cells (such as E-cadherin, *RKIP* and *RAD51*) were comparable in EZH2 knockdown cells or cells expressing EZH2 variants (Figure 6a), suggesting that their downregulation in cancer cells is a consequence rather than a cause for cellular transformation and that their expressions are not regulated by EZH2 in non-cancerous H16N2 cells when cultured on 2D surfaces. Similarly, when we further determined the molecular changes that occur in H16N2 cells expressing EZH2 variants by performing whole-transcriptome analyses with RNA sequencing (RNA-seq), the overall gene expression patterns were not much influenced by EZH2 knockdown, the expression of EZH2 variants, or changes in H3K27me3 levels. There were also only a small number of differentially expressed genes (DEGs) in EZH2 knockdown cells (MIG) or cells expressing EZH2H689A or EZH2–VAV/MT, compared to those observed in wild-type EZH2-overexpressing cells (Supplementary Figures 7a, b and Supplementary Table S1 source data for Figure 6). In contrast, EZH2ΔNLS-expressing cells displayed a very different gene expression profile (Supplementary Figures 7a, b and Supplementary Table S1 source data for Figure 6). Using the ENCODE-motifs online tool to analyze the promoters of DEGs in EZH2ΔNLS-expressing cells, we found that EZH2 target genes were highly enriched among upregulated, DEGs (23%, Figure 6b, $P = 2.3 \times 10^{-11}$, Fisher's exact test, Figure 6c), which correlates with the diminished H3K27me3 level in these cells. However, this high enrichment score was only achieved when we took all EZH2 target genes from available chromatin immunoprecipitation (ChIP) data in various cell types into account. If we only considered EZH2 targets in epithelial cells, the enrichment was substantially reduced (8%, $P = 0.0006$, Fisher's exact test, Figure 6c, red line). Taken together, these results suggest that EZH2ΔNLS-expressing cells may be losing the molecular signature of epithelial cells. Moreover, most of these upregulated genes were not de-repressed in EZH2H689A-expressing cells or EZH2 knockdown cells (Supplementary Table S1 source data for Figure 6), suggesting that EZH2ΔNLS may promote their expression through additional mechanisms other than simply alleviating H3K27-mediated repression.

Additionally, we found that a remarkably large fraction of DEGs in EZH2ΔNLS-expressing cells were highly enriched for STAT3 binding sites in their promoters (26% of upregulated genes, $P = 1.4 \times 10^{-6}$; 31% of downregulated genes, $P = 3.8 \times 10^{-14}$, Fisher's exact test, Figures 6b and c). Since we did not observe an increase in STAT3 messenger RNA or protein levels (Supplementary Table S1 source data for Figure 6 and Figures 7a–c), these results indicate elevated STAT3 activities in EZH2ΔNLS-expressing cells. Furthermore, several STAT3 target genes, including the transcription factors *STAT1*, *STAT2*, *IRF1* and *c-Fos*, were upregulated in EZH2Δn E-expressing H16N2 cells (Supplementary Table S1 source data for Figure 6). Therefore, the expressions of target genes of these transcription factors were altered and highly enriched among the DEGs as well (31% of

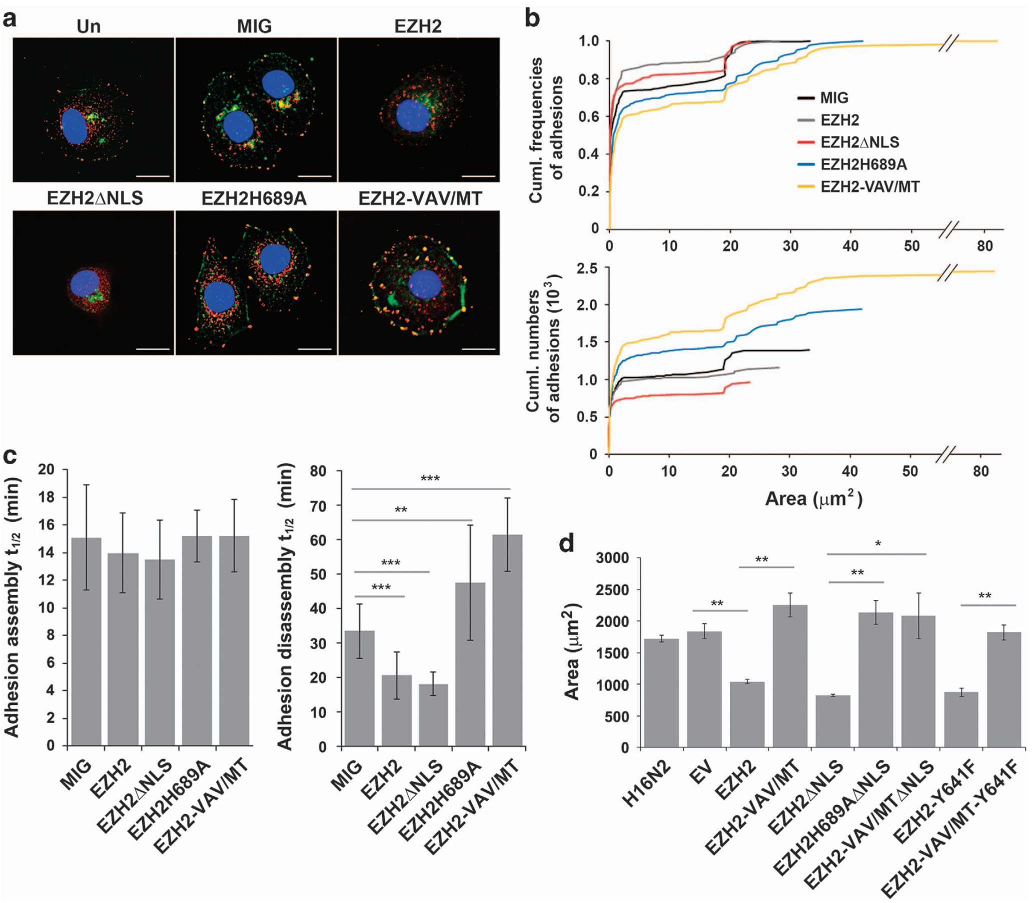

Figure 3. EZH2 promotes adhesion turnover in a VAV interaction-dependent manner. (**a**) H16N2 cells were transduced with control virus (MIG) or retroviruses for the expression of the indicated EZH2 variants and subsequently endogenous EZH2 was knocked down by shRNA. 'Un' indicates un-transduced wild-type control cells. Cells were prepared as specified in Supplementary Figure 4. Adhesion structures were visualized using a specific antibody against Paxillin (red). Phalloidin and DAPI were used to stain F-actin (green) and nuclei (blue), respectively. Scale bars, 20 μm. Representative images from one of three independent experiments are shown. Quantification of various types of adhesion structures in these cells is summarized in Supplementary Figure 4. (**b**) The empirical cumulative distribution function curve (CDF) shows the direction of the changes in the size of adhesion structures in H16N2 cells expressing EZH2 variants as in **a**. The adhesion structures were determined by Paxillin staining. Kolmogorov–Smirnov tests were performed between groups using online software (http://www.wessa.net/rwasp_Reddy-Moores%20K-S%20Test.wasp). The *P*-values are all <0.00001. The graph in the lower panel shows cumulative (cumul.) numbers of adhesion structures in each group. Representative results from one of the three independent experiments with 60 cells per group are shown. (**c**) H16N2 cells expressing EZH2 variants, as in **a**, were transfected with plasmids to express mCherry-Paxillin and plated on fibronectin-coated glass slides, then analyzed by time-lapse live imaging. Half-life values of adhesion assembly and disassembly were calculated based on mCherry-Paxillin signal, as described.[81] Data represent means ± s.d. of 15 adhesions on 4–5 cells per group. Two-tailed Student's *t*-test with equal variance, $^{**}P=0.007$, $^{***}P=6.4\times10^{-9}$, 1.4×10^{-7}, 4.4×10^{-5} (top to bottom). (**d**) H16N2 cells were left un-transfected or co-transfected with EZH2 shRNA and empty vector (EV) or vectors to express variants of EZH2–GFP protein. Cell spreading of GFP positive cells, compared to cells transduced with EV, was quantified. At least three experiments and more than 20 cells were scored for each group in each experiment. Data represent means ± s.e.m. Two-tailed Student's *t*-test with equal variance, $^{**}P=0.0006$, 0.0007, 0.002, 0.0005 (left to right), $^{*}P=0.03$.

upregulated genes, Fisher's exact test, $P=2.9\times10^{-9}$; 35% of downregulated genes, Fisher's exact test, $P=5.5\times10^{-17}$, Figures 6b and c). However, the prominent oncogene, *MYC*, was downregulated, while several MYC inhibitors, such as *Id2*, *Mxi1* and *Mxd4*, were upregulated in cells expressing EZH2ΔNLS (Supplementary Table S1 source data for Figure 6).[44–46] Consequently, most of the downregulated genes are known MYC target genes (73%, $P=4.1\times10^{-50}$, Fisher's exact test, Figures 6b and c). Even though the downregulation of *MYC* may appear to be counterintuitive given the elevated oncogenic capacity of EZH2ΔNLS, the expression of a constitutively active STAT3 mutant in mesenchymal stem cells has also been shown to downregulate MYC.[47] Reduced *MYC* expression may have also directly resulted in the observed downregulation of several tumor suppressors, such as *BRCA1*, *XRCC2*, *NF2*, *FH* and *RASSF1*, in EZH2ΔNLS-expressing cells (Supplementary Table S1 source data for Figure 6).

EZH2 promotes STAT3 activity and cellular transformation through methylation of Talin1

The increased activities of STAT family proteins and the reduced expressions of tumor suppressors are associated with cancer cell survival and growth[48] and are therefore likely to contribute, in large part, to the elevated oncogenic activity of EZH2ΔNLS. Since overexpression of EZH2 is reported to activate STAT3 through methylation,[12,49] we wondered whether EZH2-mediated STAT3 methylation is dependent on its interaction with VAV. Surprisingly, we found that EZH2-mediated STAT3 methylation did not show obvious changes in cells expressing EZH2 variants (Figure 7a, with quantification shown in Supplementary Figure 7c), suggesting that STAT3 methylation is unlikely to play a role in this context. The residual STAT3 methylation observed in EZH2H689A-expressing cells is expected (Figure 7a), since STAT3 is also methylatable by SET9.[50] However, phosphorylation of STAT3 on Tyr 705 (pY705) by JAK2, which is required for STAT3 dimerization and activation, was increased in cells expressing wild-type EZH2 and substantially elevated in cells expressing EZH2ΔNLS, while phosphorylation of this site was diminished by the disruption of EZH2 interaction with VAV (Figure 7b and Supplementary Figure 7d). In contrast, phosphorylation of Ser 727 (pS727) on STAT3 by ERK MAP kinase[51] was not affected by the expression of EZH2 variants (Figure 7b). Furthermore, VAV interaction was specifically required for EZH2 or cytosolic EZH2-promoted phosphorylation of Y705,

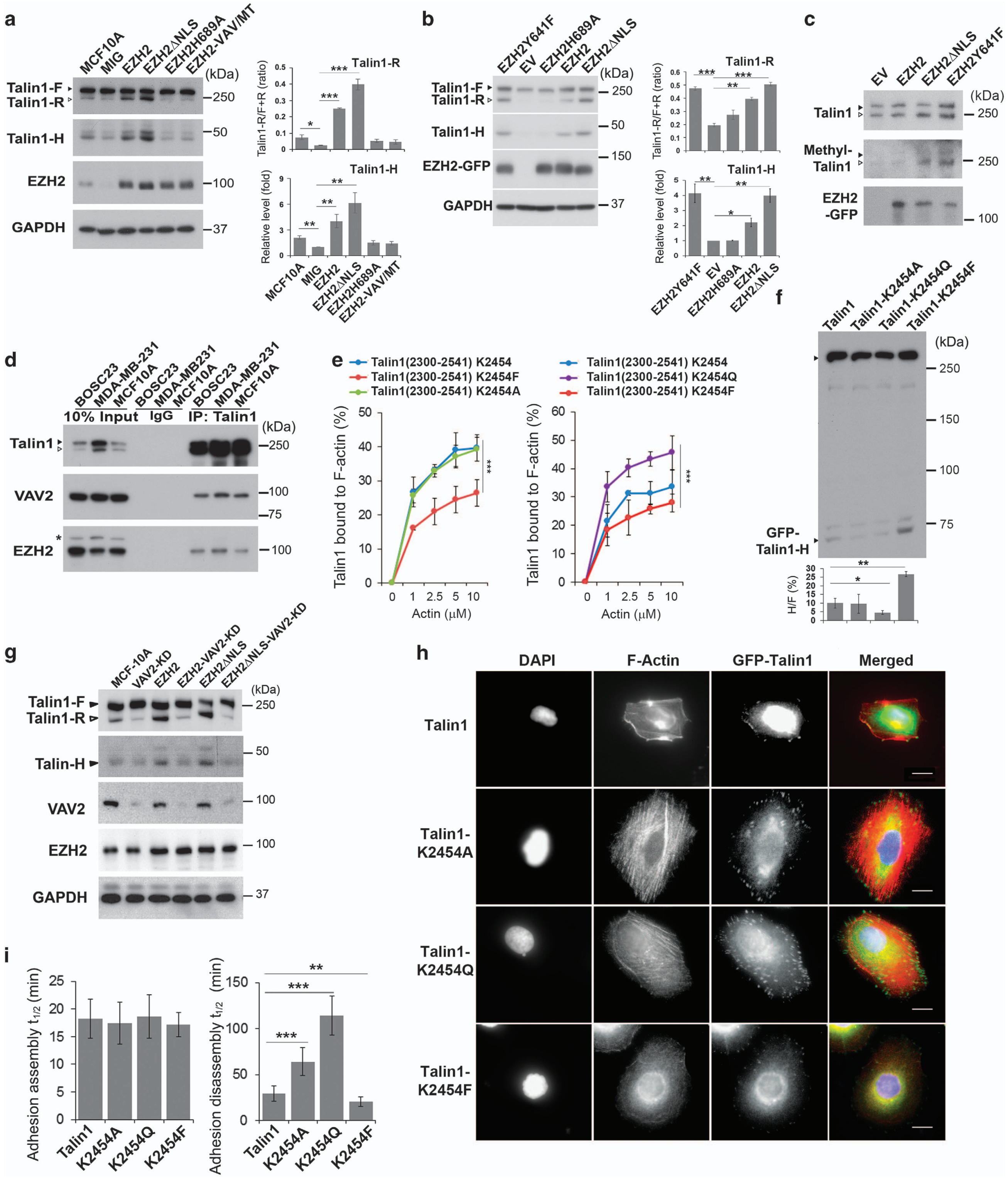

but was dispensable for IL-6-stimulated STAT3 activation (Figure 7c), suggesting a cytokine-independent, novel STAT3 activation signaling pathway mediated by cytosolic EZH2.

Since interaction with VAV is also required for EZH2-mediated Talin methylation, we sought to determine whether the methylation state of Talin1 could also have an effect on STAT3 activation. Indeed, expression of the tri-methyl-mimicking Talin1 mutant (K2454F) was sufficient to stimulate substantial STAT3 phosphorylation (pY705) and activation (Figure 7d and Supplementary Figures 7e, f). Moreover, EZH2-, EZH2ΔNLS- and methyl-Talin mutant-promoted STAT3 phosphorylation was dependent on JAK2 activity (Figure 7b and Supplementary Figure 7f). Consequently, similar to EZH2 and EZH2ΔNLS, the methyl-mimicking Talin1 mutant also significantly promoted cellular transformation (Figure 7e) that was dependent on JAK/STAT activity (Figure 7f). Furthermore, the expressions of several key factors that were upregulated in EZH2ΔNLS-expressing cells were also upregulated by methyl-mimicking Talin1 (Figure 7g). Overall, our data suggest that cytosolic EZH2 contributes to the initiation of cellular transformation or the formation of cancer stem cells through VAV-dependent Talin methylation and STAT3 activation.

EZH2 is enriched in the cytoplasm of human breast cancer stem cells

To validate the physiological relevance of cytosolic EZH2 in human breast cancer cells, we first sorted MDA-MB-231 human triple-negative breast cancer cells based on their surface expression levels of CD44 and their capacity to efflux Rhodamine 123 dye, and then analyzed the sub-cellular distribution of EZH2 in the sorted cells. We found that EZH2 was significantly enriched in the cytoplasmic compartment of $CD44^{High}$ Rhodamine 123 negative cancer stem cells with the side population phenotype ($CD44^{Hi}SP$) (Figures 8a–c and Supplementary Video 5), whereas cytosolic EZH2 was largely depleted in $CD44^{Low}$ Rhodamine 123 positive cells ($CD44^{Lo}Rd^{+}$) (Figures 8a–c and Supplementary Video 6). Correspondingly, $CD44^{Hi}SP$ cells exhibited higher STAT3 activity than $CD44^{Lo}Rd^{+}$ cells (Figure 8c). Taken together, our results suggest a cytosolic role for EZH2 in cellular transformation, likely through methylation of Talin and the activation of STAT3 in human breast cancer stem cells. It is also possible that cytosolic EZH2 contributes to the generation of tumor-initiating cells partly by amending their adhesion properties.

DISCUSSION

Here, we report that the polycomb group protein, EZH2, promotes cellular transformation and metastasis through VAV interaction-dependent mechanisms. While EZH2 lacking its NLS exhibited much greater transforming capacity than wild-type EZH2, targeted disruption of EZH2 interaction with VAV abolished both wild-type EZH2- and EZH2ΔNLS-promoted cellular transformation. Because the well-established VAV effector functions are relatively unaffected by the absence of EZH2 or the expression of EZH2 variants, we believe that VAV is likely acting as an adapter in this context. We have shown that EZH2–VAV interaction is critical for EZH2's recruitment to Talin and subsequent Talin methylation-promoted adhesion turnover. Furthermore, EZH2–VAV interaction may also bring JAK2 into close proximity with EZH2-interacting STAT3, thereby promoting phosphorylation of STAT3. We hypothesize that both of these VAV interaction-dependent events (adhesion turnover and STAT3 activation) are critical for EZH2-mediated tumorigenic signaling (see model in Supplementary Figure 8).

Mechanistically, EZH2 is not involved in the EGF signaling pathway, a key factor in most epithelial malignancies.[52] EGF-stimulated VAV2 activation and downstream signaling events, including activation of VAV effectors, were not affected by EZH2 knockdown or overexpression of EZH2 variants. Moreover, even though cytosolic EZH2-expressing cells possess high oncogenic capacity, the expression of several well-characterized tumor suppressors that are repressed by EZH2 in cancer cells were not regulated by EZH2 in mammary epithelial cells. Instead, our data suggest that EZH2–VAV2 interaction controls adhesion turnover and cellular transformation through Talin1 methylation and

Figure 4. EZH2-mediated Talin1 methylation regulates adhesion dynamics in mammary epithelial cells. (**a**) Whole-cell extracts of EZH2 knockdown MCF10A cells transduced with control (MIG) or retrovirus to express the indicated EZH2 variants were analyzed by immunoblotting. GAPDH immunoblot served as a loading control. The expression levels of EZH2 in EZH2 knockdown (MIG) or EZH2 variant-expressing cells were controlled in Supplementary Figure 5a. Quantifications of Talin1 Rod domain (Talin1-R) were done by setting Talin1 full length (Talin1-F) plus Talin1-R signal as one and the ratios (Talin1-R/F+R) are shown in the upper bar graph. The relative abundance of head domain (Talin1-H) normalized to the level of Talin1-F is shown in lower bar graph. The amount of Talin1-H in empty vector (EV) control cells was set as 1. Data represent means ± s.e.m. from three independent experiments. Two-tailed Student's *t*-test with equal variance, $*P = 0.018$, $**P = 0.006$, 0.009, 0.003, $***P = 0.0002$, 3.3×10^{-7} (top to bottom). (**b**) BOSC23 cells were transfected with EV or plasmids to express the indicated EZH2 variants. Whole-cell extracts were isolated by lysing the cells directly on the culture plates to avoid any mechanical force-induced Talin cleavage and analyzed by immunoblotting. Talin1-R and Talin1-H levels were quantified as described in **a**. Data represent means ± s.e.m. from three independent experiments. Two-tailed Student's *t*-test with equal variance, $*P = 0.01$, $**P = 0.0002$, 0.007, 0.003, $***P = 6.7 \times 10^{-5}$, 3.8×10^{-5} (top to bottom). (**c**) Talin1 from BOSC23 cells expressing EZH2 variants was immunoprecipitated and Talin1 methylation was determined by pan-methyl-lysine antibody. ($n > 3$). (**d**) Talin1 was immunoprecipitated from BOSC23, MDA-MD-231 or MCF10A cytosolic extracts and the association of EZH2 with VAV2 was determined by immunoblot using specific antibodies. *Background band detected by EZH2 antibody at ~120 kDa. ($n > 3$). (**e**) Recombinant Talin1 (2300–2452) containing the C-terminal actin-binding site was purified and incubated with F-actin. Binding of Talin1 mutants to F-actin was determined using actin-co-sedimentation assays. Data represent means ± s.d. ($n = 3$). Two-factor ANOVA with replication, $***P = 4.9 \times 10^{-31}$, 2×10^{-32} (left to right). (**f**) N-terminal GFP-fusion proteins of Talin1 variants (methyl-mimicking Talin1-K2454F or unmethylatable Talin1-K2454A or Q) transiently expressed in BOSC23 cells were detected by immunoblotting with anti-GFP antibody. Rod domain derived from cleaved GFP-Talin1 is indistinguishable from endogenous Rod domain, and is not detectable by anti-GFP antibody. The bar chart shows the average percentage of cleaved head domain 'H' relative to full-length GFP-Talin1 'F' ($n = 3$). Data represent means ± s.d. Two-tailed Student's *t*-test, $**P = 0.0008$, $*P = 0.03$. (**g**) Wild-type MCF10A cells were either left untreated or transduced with retrovirus to express wild-type EZH2 (EZH2), cytosolic EZH2 (EZH2ΔNLS) or VAV interaction mutant EZH2 (EZH2–VAV/MT). VAV2 knockdown was achieved by additional transduction with VAV2-specific shRNA-expressing lentivirus. Data shown are representative of two independent experiments. (**h**) H16N2 cells were transduced with retroviruses to express GFP-Talin1 variants. Adhesion structures and F-actin were visualized with anti-GFP antibody (green) and phalloidin (red), respectively. Representative images from one of more than three experiments are shown. Scale bar, 20 μm. Quantification of adhesion structures in H16N2 cells expressing GFP-Talin1 variants is shown in Supplementary Figures 5f, g. (**i**) H16N2 cells expressing Talin1 variants were analyzed as in Figure 3c and half-life values of adhesion assembly and disassembly were calculated based on GFP-Talin1 signal. Data represent means ± s.d. of 10–15 adhesions in 4–5 cells per group. Two-tailed Student's *t*-test with equal variance, $**P = 0.001$, $***P = 5 \times 10^{-14}$, 2.5×10^{-8} (top to bottom) ($n > 3$).

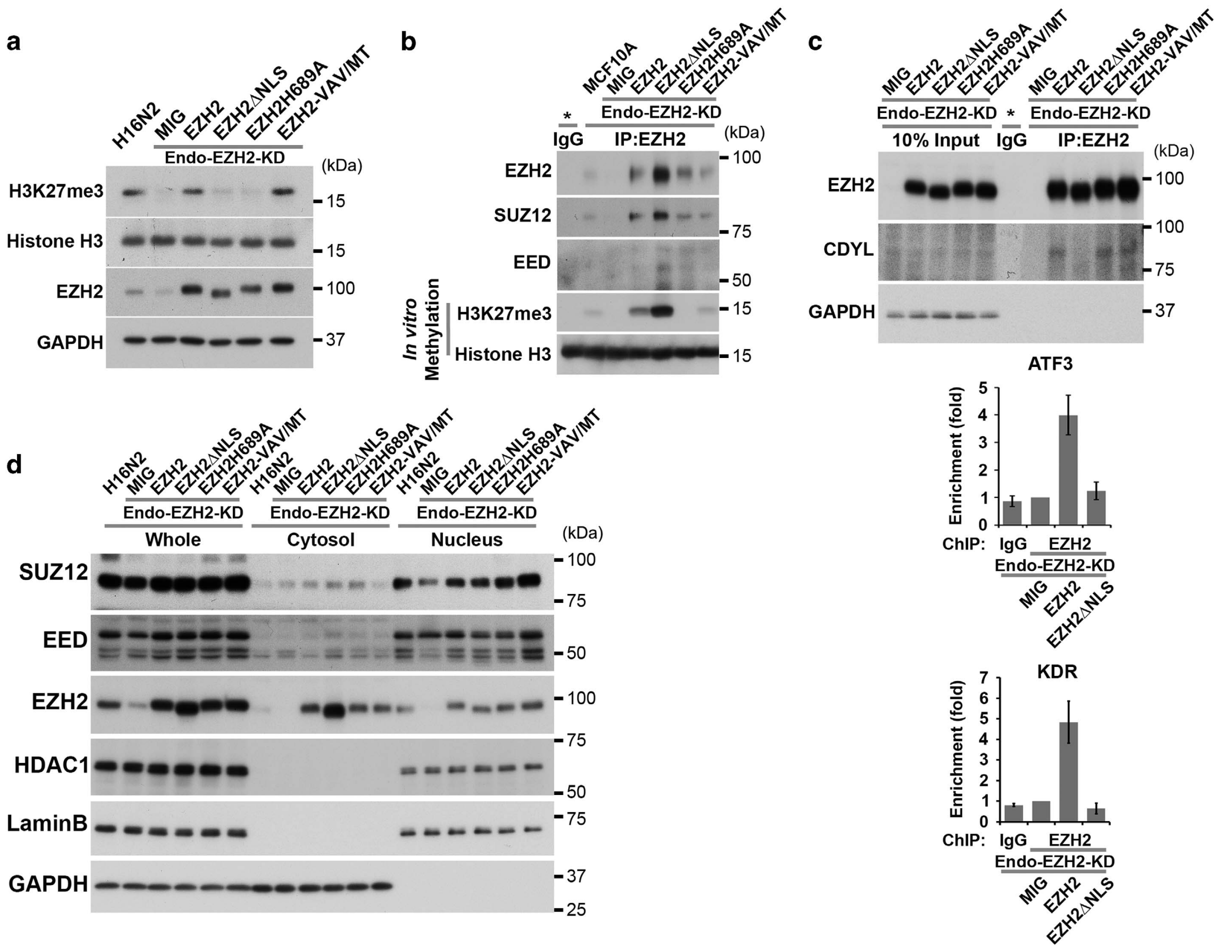

Figure 5. PRC2 activity and sub-cellular distribution in EZH2 variant-expressing H16N2 cells. (**a**) H3K27me3 levels in H16N2 cells (as in Figure 2a) were determined by immunoblotting whole-cell extracts. GAPDH served as a loading control. ($n = 3$) (**b**) EZH2 was immunoprecipitated from the cytosolic extracts of EZH2 knockdown MCF10A cells reconstituted with EZH2 variants and the association with SUZ12 and EED was determined by immunoblot analyses. *In vitro* methylation activity of immunoprecipitated EZH2 toward histone octamers was detected by H3K27me3-specific antibody. The sub-cellular fractionation was controlled in Supplementary Figure 6. ($n > 3$). (**c**) The interaction of EZH2 variants with CDYL and recruitment to EZH2 target genes was determined. EZH2 variants were immunoprecipitated from H16N2 cells to detect their interaction with CDYL (upper panel). Chromatin immunoprecipitation (ChIP) from cells expressing EZH2 variants was performed using EZH2-specific antibody. Enrichments of EZH2 variants on the promoters of *ATF3* and *KDR*, compared to IgG control, were determined by qPCR. Data represents means ± s.d. of technical triplicates. Representative results from two independent experiments are shown. Asterisks in **b** and **c** indicate IgG controls using cytosolic extracts of EZH2ΔNLS-expressing cells. (**d**) Subcellular distributions of PRC2 components were analyzed by immunoblot analyses of whole cell, cytosolic and nuclear extracts isolated from H16N2 cells expressing EZH2 variants. Proper sub-cellular fractionation was controlled by blotting for GAPDH (cytosol) and Lamin B (nucleus) ($n = 3$).

cleavage. In fact, elevated focal adhesion remodeling of cells *in vitro* is frequently correlated with elevated migratory rate and metastatic capacity *in vivo*. Furthermore, over 90% of all cancers originate from mutations in epithelial cells,[53] therefore, changes in adhesion properties of these cells are particularly critical for tumor initiation, progression and metastasis.[54,55] In this context, EZH2 and methylated Talin specifically regulate adhesion turnover, but do not affect adhesion formation. These changes in adhesion properties may also directly contribute to the oncogenic capacity of epithelial cells by amending their gene expression patterns.[56,57]

Interestingly, aside from altered adhesion properties, STAT3 activity in cytosolic EZH2-expressing cells was also significantly elevated. Members of the STAT family of proteins are known to transiently regulate gene expression in response to cytokines and growth factors. Constitutively, activated STAT3 is also found in more than 50% of primary breast tumors and tumor-derived cell lines.[58] In addition to the direct contribution of activated STAT3 to the elevated oncogenic capacity of EZH2ΔNLS-expressing cells, subsequent upregulation of STAT1/2 by STAT3 is likely to be responsible for the increased expressions of various claudins and MMPs that are associated with heightened metastatic capabilities.[59,60]

Our data also revealed that JAK2 activity was critical for EZH2- and methyl-mimicking Talin mutant-promoted STAT3 phosphorylation (pY705) and activation. JAK2 has been reported to interact with VAV1 in myeloid cells[61] and may also associate with VAV2 in epithelium or breast cancer cells to implement EZH2-promoted STAT3 activation. Indeed, EZH2's capacity to interact with VAV was found to be essential for EZH2-, but not IL-6-promoted STAT3 phosphorylation, suggesting a specific, novel role for VAV in EZH2-promoted STAT3 activation during cellular transformation. Interestingly, EZH2-mediated STAT3 methylation is not dependent on EZH2's interaction with VAV2. However, the two reported EZH2-mediated STAT3 methylation sites[12,49] are likely to fine tune the conformation of STAT3, making it more

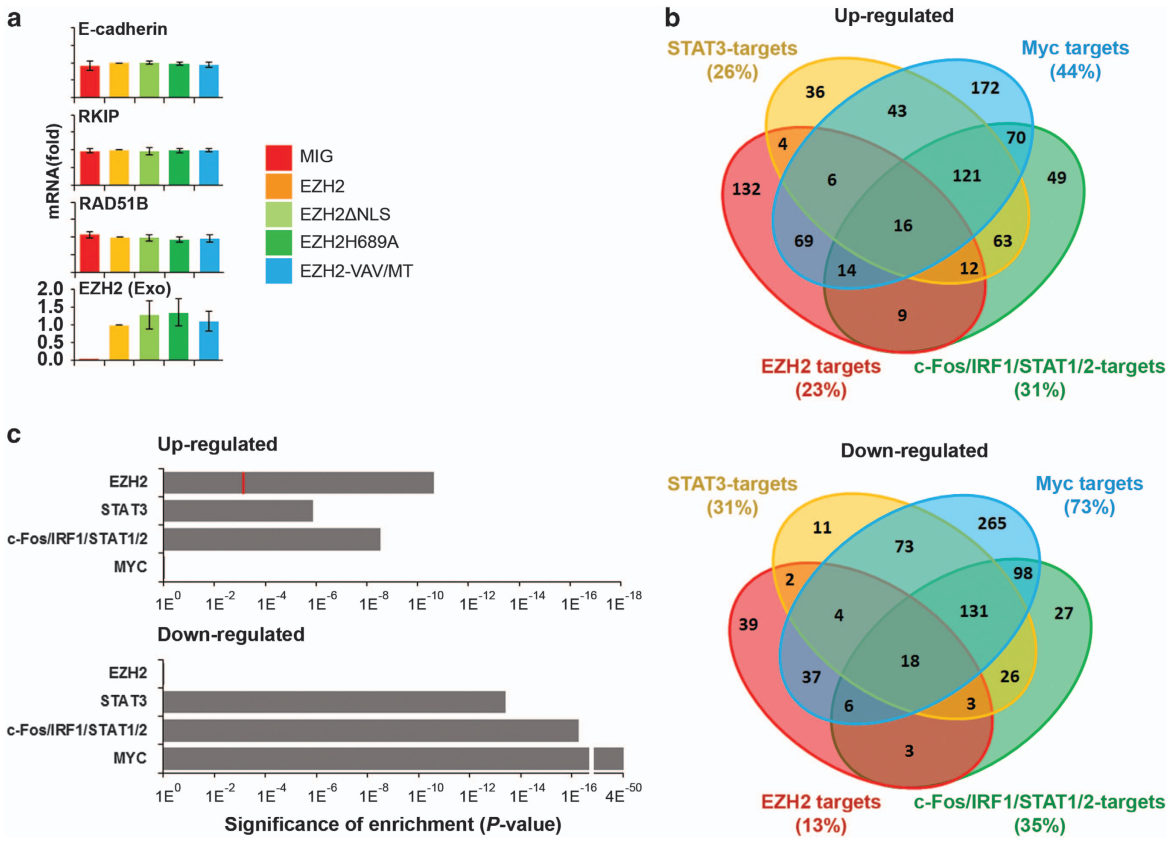

Figure 6. EZH2ΔNLS regulates the expression of STAT target genes. (**a**) Transcript levels of tumor suppressors reported to be regulated by EZH2 in various cancer cells were determined by RT-qPCR and normalized against GAPDH. Data represent means ± s.d. of three independent experiments with technical triplicates. (**b**, **c**) The differentially expressed genes between EZH2ΔNLS- and wild-type EZH2-overexpressing cells identified in RNA-seq experiments (full RNA-seq data sets are shown in Supplementary Figures 7a, b and Supplementary Table S1 source data for Figure 6) were analyzed to show the numbers (**b**) or enrichment *P*-values (**c**) of regulated genes that are targets of the indicated transcriptional regulators. Transcription factor binding sites within the potential transcriptional regulatory region (2 kb upstream and 0.5 kb downstream of the transcriptional start site) were determined using the ENCODE online tool (http://encodeproject.org/ENCODE/). Venn diagram in **b** shows the numbers of overlapping target genes of EZH2, MYC, STAT3 (direct), and the target genes of proteins upregulated by STAT3 (STAT1, STAT2, c-Fos and IRF1). Red bar in **c** indicates the enrichment *P*-value of the differentially expressed EZH2 target genes among reported epithelial EZH2 targets. Target gene enrichment was determined using the Fisher's exact test (assuming all protein coding genes = 20 274). Detailed gene lists used for **b**, **c** are shown in the Supplementary Table S1 source file for Figure 6 and the raw data from the RNA-seq experiments that have been deposited to an online data base (ArrayExpress website). For reviewer's access see Materials and methods section.

accessible for phosphorylation and final activation, as demonstrated by reduced STAT3 (pY705) in EZH2H689A-expressing cells. Overall, elevated STAT3 signaling is likely to be critical for the enhanced transforming capacity of EZH2 and cytosolic EZH2 in our experimental setting.

In addition, genes implicated in promoting epithelial–mesenchymal transition or those expressed in cancer stem cells, such as *CD44*, various *ALDHs*, *KLF8*, *S1PR1*, *Bmi1*, *CCL5*, *ZEB2* and *SNAI1* were upregulated in cells expressing EZH2ΔNLS. We also found that cytoplasmic EZH2 was enriched in human breast cancer stem cells. Consistent with our results, abundant EZH2 in the cytosol has been reported to associate with primary human glioma stem-like cells.[62] Collectively, cytosolic EZH2-promoted adhesion turnover through Talin1 methylation and STAT3 activation may promote the initiation of epithelial–mesenchymal transition and cancer stem cell formation before the establishment of oncogenic transcriptional programs by nuclear EZH2.

The enormous effort that has been put into developing EZH2-specific methyltransferase inhibitors as anticancer drugs, including DZNep,[63] GSK126[(ref. 64)] and the specific compound, EPZ005687[(ref. 65)], have yielded promising results in laboratory or pre-clinical settings[66,67] and several specific drugs targeting EZH2 and other epigenetic regulators are currently in clinical trials.[68,69] However, the clinical application of these drugs should be tested with caution. Our previous studies have shown that EZH2 plays indisputable roles in lymphocyte development and function,[22,70] and several studies also reveal that EZH2 is crucial for the maintenance of various somatic stem cells including skin, muscle, hematopoietic and neural stem cells.[20,71–74] Additionally, tumor suppressor and methyltransferase-independent functions of EZH2 in tumorigenesis have been suggested recently.[9,16–18] Prolonged EZH2 depletion has also been recently reported to lead to an epigenetic switch in cancer cells that results in enhanced tumor progression.[75] Similarly, deletion of *Ezh2* gene in mice could result in genome instability making Ezh2-deficient cells more susceptible for other oncogene-induced tumorigenesis.[76] Moreover, treatment with an EZH2 inhibitor, such as DZNep or GSK126, has been proven ineffective on glioma stem-like cells[62] and has been shown to restrict anti-tumor immunity of cytotoxic T cells.[77] For these reasons, EZH2-specific methyltransferase inhibitor-based cancer treatments may not be the best strategy to combat EZH2-associated cancers.

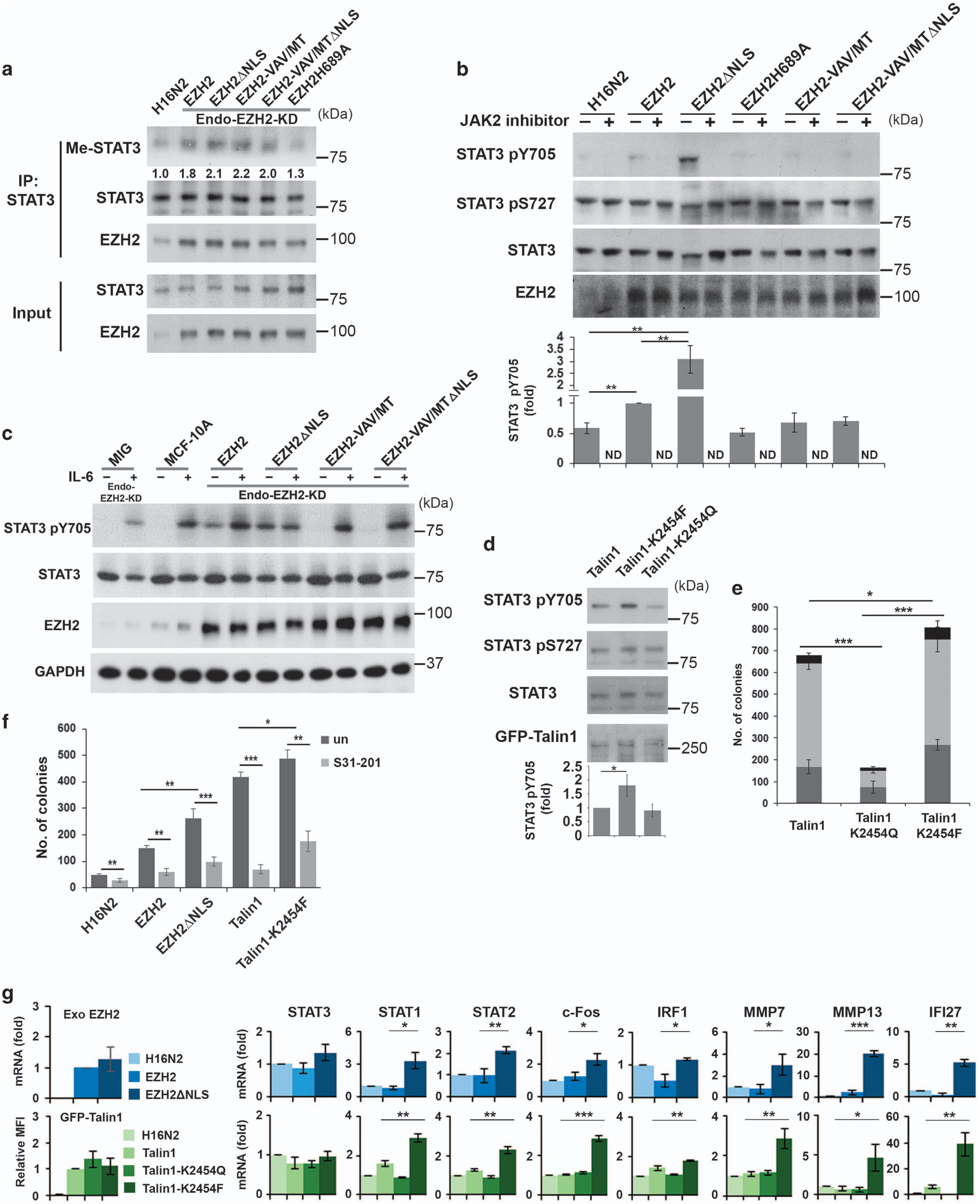

In summary, the data reported here demonstrate that the polycomb group protein, EZH2, in addition to its well-established roles in epigenetic silencing of tumor suppressors,[78–80] also controls cellular transformation and tumor growth through VAV interaction-dependent Talin1 methylation. Nuclear functions of EZH2 are frequently involved in regulating basic cell survival and proliferation, whereas cytosolic pathways are more specific for fine tuning protein functions in certain physiological or pathological contexts. By targeting the extra-nuclear functions of EZH2 through the disruption of the

Figure 7. EZH2-mediated Talin1 methylation promotes STAT3 activation and cellular transformation. (**a**) STAT3 immunoprecipitated from H16N2 cells-expressing EZH2 variants (as in Figure 2a) was analyzed for methylation by pan-methyl-lysine antibody. Endo-EZH2-KD denotes knockdown of endogenous EZH2. Numbers below the Me-STAT3 immunoblot indicate the relative fold change after normalization to the immunoprecipitated STAT3 amounts. The abundance of Me-STAT3 in H16N2 cells was set as 1. Further quantifications are shown in Supplementary Figure 7c ($n = 3$ or 4). (**b**) Immunoblots for phospho-STAT3 in extracts of H16N2 cells expressing EZH2 variants (treated with or without JAK2 inhibitor III SD-1029). The bar chart below the immunoblots shows the amounts of STAT3 pY705 in the indicated cells compared to the amounts observed in EZH2-expressing control cells after normalization to total STAT3. ND, not determined. Data represent means ± s.e.m. Two-tailed Student's *t*-test with equal variance, $^{**}P = 0.0018$, 0.0033, 0.0012 (top to bottom), $n = 3$. (**c**) Wild-type (MCF10A) or endogenous EZH2 knockdown MCF10A cells transduced with control virus (MIG) or retrovirus to express the indicated EZH2 variants were stimulated with or without IL-6 for 30 min. Whole-cell extracts were subjected to immunoblotting with antibodies against STAT3 pY705 and total STAT3 (pY99). GAPDH served as a loading control. Data shown are representative of three independent experiments. (**d**) Immunoblots for phospho-STAT3 in extracts of H16N2 cells expressing Talin1 variants. The bar chart below the immunoblots shows the amounts of STAT3 pY705 in the indicated cells compared to the amounts observed in Talin1 expressing control cells after normalization to total STAT3. $^{*}P = 0.04$, $n = 4$. (**e**) H16N2 cells overexpressing Talin1 variants were analyzed for anchorage-independent cell growth as in Figure 2a, except that the colonies were also scored according to their size. Black: $>60\,000\ \mu\text{m}^2$, light gray: $10\,000$–$60\,000\ \mu\text{m}^2$, dark gray: 4000–$10\,000\ \mu\text{m}^2$. Data represent means ± s.d. ($n = 3$). Two-tailed Student's *t*-test with equal variance, $^{*}P = 0.03$, $^{***}P = 0.0001$, 0.00004, (top to bottom). (**f**) EZH2 knockdown H16N2 cells transduced with retrovirus to express the indicated EZH2 variants (EZH2, EZH2ΔNLS) or wild-type H16N2 cells un-transduced (H16N2) or transduced to express Talin1 variants (Talin1, Talin1-K2454F) were tested for anchorage-independent cell growth. Cells were grown in medium untreated (un) or containing 200 µM of STAT3 inhibitor (S31–201) for 24 h before culture in soft agar. Data represent means ± s.d. ($n = 3$, three independent experiments with technical triplicates). Two-tailed Student's *t*-test with equal variance, $^{*}P = 0.03$, $^{**}P = 0.0004$, 0.0003, 0.0002, 0.01, $^{***}P = 0.000097$, 0.00004 (top to bottom). (**g**) Gene expression profiles of selected genes in H16N2 cells expressing EZH2 (blue shades) or Talin1 variants (green shades). The expression levels of exogenous EZH2 variants (Exo EZH2), Talin1 variants (GFP-Talin1) and indicated genes were measured by RT-qPCR or mean fluorescence intensity (MFI) of FACS analysis (Talin1 variants). Data represent means ± s.d. ($n = 3$). Two-tailed Student's *t*-test with equal variance, $^{*}P = 0.02$, 0.02, 0.03, 0.04, $^{**}P = 0.01$, 0.0005, $^{***}P = 0.00006$ (top, left to right). $^{*}P = 0.02$, $^{**}P = 0.0007$, 0.0005, 0.007, 0.003, 0.004, $^{***}P = 0.00004$ (bottom, left to right).

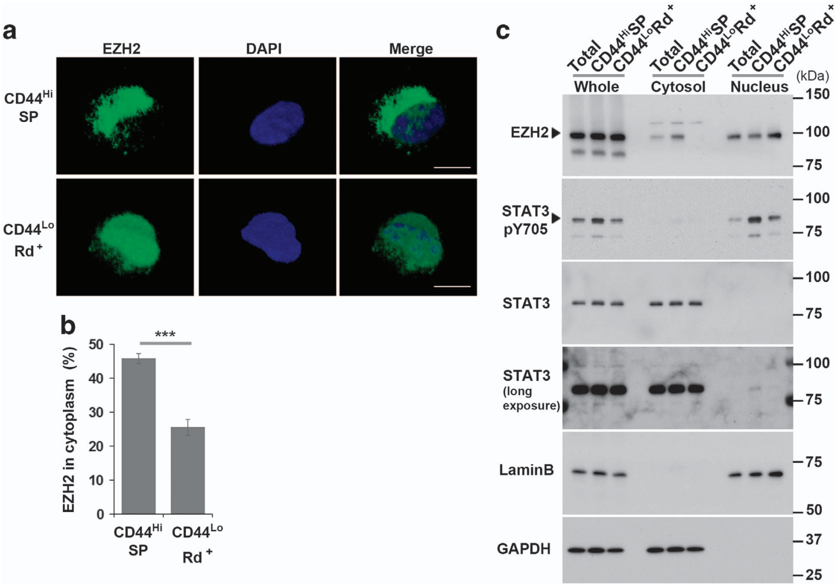

Figure 8. EZH2 is enriched in the cytoplasm of cancer stem cells. MDA-MB-231 cells were analyzed based on their surface expression levels of CD44 (high or low) and their ability to efflux Rhodamine 123 dye. CD44 high and Rhodamine 123 negative cells were defined as cancer stem cells with the side population (SP) phenotype (CD44$^{\text{Hi}}$SP). CD44$^{\text{Hi}}$SP and CD44 low Rhodamine positive (CD44$^{\text{Lo}}$Rd^{+}) cells were also sorted from cultured MDA-MB-231 cells. EZH2 in the cells was visualized by immunofluorescent staining with specific antibody. (**a**) Representative 3D reconstructed *z*-stack confocal microscopy images from two independent experiments are shown. Scale bars, 10 µm. (**b**) Percentage of EZH2 in the cytoplasm was quantified based on the immunofluorescent signal of EZH2. Data represent means ± s.e.m. ($n > 30$ pooled from two independent experiments). $^{***}P = 1.1 \times 10^{-10}$. (**c**) Subcellular distributions of EZH2 and STAT3 (phosphorylated and total) were analyzed by immunoblot analyses of whole cell, cytosolic and nuclear extracts isolated from different subpopulations of MDA-MB-231 cells. Proper subcellular fractionation was controlled by blotting for GAPDH (cytosol) and Lamin B (nucleus).

EZH2–VAV interaction, we may be able to effectively control cancer progression without eliciting serious resistance. In the clinical setting, disruption of EZH2 interaction with VAV in circulating and disseminated tumor cells may result in migratory arrest of the tumor cells, similar to results observed in Ezh2-deficient leukocytes, by forming abnormally stable adhesions with the microvascular wall[37] and rendering them unable to transmigrate into interstitial tissues and establish metastases. Thus, our findings not only identify a unique regulatory role of EZH2 in tumorigenesis, but also provide a mechanistic basis for developing novel therapeutic intervention strategies in the treatment of human cancers associated with EZH2 overexpression or drug resistant stem-like tumor cells.

MATERIALS AND METHODS

Recombinant protein production

VAV$_{1-172}$ was cloned into PGEX-4T and EZH2$_{201-252}$ was cloned into pET-21b. The VAV1 fragment was derived from human complementary DNA (cDNA). The EZH2 fragment was derived from mouse cDNA, however, the amino-acid sequence of the relevant domain is highly conserved between human and mouse. They were grown and expressed in BL21 (DE3) cells to an OD$_{600}$ of 0.6 at 37 °C and induced with 1 mM IPTG for 3 h. GST–VAV was purified using Glutathione Sepharose beads and EZH2–His was purified using His-Pur Cobalt resin. Individual mutations in EZH2$_{201-252}$ were created using the Stratagene Quik change site-directed mutagenesis using primers as described and were then purified.

Cell culture and plasmids

HEK-293 cells used for expression of full-length EZH2 were cultured in DMEM supplemented with 10% FCS. Jurkat T-cells were grown in RPMI medium containing 10% fetal calf serum (FCS) and were used for immunoprecipitation of endogenous VAV1. H16N2 and MCF10A mammary epithelial cells lines were grown in supplemented F-12 or DMEM media. Cells were transfected with MSCV-IRES-GFP (MIG) vector-based retroviruses encoding EZH2, EZH2 lacking its nuclear localization signal-RKKKRK (EZH2ΔNLS), enzymatically inactive EZH2 (EZH2H689A) or the EZH2–VAV interaction mutant (EZH2–VAV/MT or EZH2–VAV/MTΔNLS). Cells were sorted based on their expression of GFP by FACS-ARIA. Endogenous EZH2 was knocked down using shRNA against *EZH2* (V2LHS_17509, Open Biosystems, Huntsville, AL, USA) and selected with puromycin (1 μg/ml). The shRNA target nucleotides on *EZH2* cDNA were mutated (1910-5′ tctcagaatactgtggggacatgatttctcaggatgaagcag 3′1951, bold underlined letters are mutated.). MDA-MB-231 cells for mammary tumor xenografts were grown in DMEM supplemented with 7.5% FCS. Cells expressing EZH2 or variants (as described) were obtained using retrovirus-mediated expression (as described) followed by cell sorting based on their GFP expression using FACS-ARIA.

Immunoprecipitation

EZH2–HIS$_{201-252}$ and EZH2 with individual mutations were immobilized on the His-Pur Cobalt resin and allowed to interact overnight with GST–VAV$_{1-172}$ or GST alone (control) in phosphate-buffered saline (PBS) buffer pH 7.4. Following this, the beads were extensively washed and subject to sodium dodecyl sulfate–polyacrylamide gel electrophoresis (SDS–PAGE) and western blot analysis using anti-His (h-3) and anti-GST (B-14) antibodies from Santa Cruz (Santa Cruz, CA, USA) to analyze the EZH2–VAV complex. To determine the interaction between full-length EZH2 and VAV, VAV1 protein was immunoprecipitated from the cytosolic fraction of Jurkat cells with α-VAV1 (C14) antibody from Santa Cruz and immobilized on Protein G Sepharose. Similarly, Flag-tagged EZH2 WT or EZH2 with individual mutations were immunoprecipitated from HEK-293 cells with α-Flag (M2) antibody from Sigma (Sigma-Aldrich, St Louis, MO, USA) and Protein G Sepharose beads. They were then eluted from the beads by using a competing FLAG peptide. Equal quantities of the WT EZH2 or EZH2 with individual mutations were incubated overnight with VAV1 in a BC-100 buffer. The beads were then extensively washed and analyzed by western blotting with α-EZH2 (N-20) antibodies from Santa Cruz and VAV-specific antibodies.

Immunoblotting and antibodies

Immunoblotting was performed according to standard protocols with the following antibodies; EZH2 (D2C9, Cell Signaling, Boston, MA, USA), EED (AA19, Millipore, Darmstadt, Germany), SUZ12 (Ab12073, Abcam, Cambridge, UK), CDYL (ab5188, Abcam), Actin (C-11, Santa Cruz), VAV2 (EP1067Y, Abcam), VAV pY174 (sc-16408-R, Santa Cruz), H3 (ab1791, Abcam), H3k27me3 (07-449, Abcam), STAT3 (F2, Santa Cruz), STAT3 pY705 (D3A7, Cell Signaling), STAT3 pS727 (ab30647, Abcam), EGFR (sc-03-G, Santa Cruz), EGFR pY1173 (sc-12351-R, Santa Cruz), AKT1/2 (N-19, Santa Cruz), AKT pS473 (193H12, Cell Signaling), Tubulin (AA13, Santa Cruz), LaminB (C-20, Santa Cruz), Talin1, N-terminal (TA205, Millipore), Talin1 (also used for IP, 8d4, Santa Cruz), Talin1 pS425 (5426S, Cell Signaling), FAK (2601P, Cell Signaling), FAK pY397 (3283S, Cell Signaling), FAK pY925 (3284S, Cell Signaling), FAK pY576/577 (3281S, Cell Signaling), GAPDH (6C5, Ambion, Austin, TX, USA), pan-methyl-lysine (ab3715, Abcam), Src (32G6, Cell Signaling), Src pY416 (D49G4, Cell Signaling), Src pY527 (2105P, Cell Signaling), ERK (137F5, Cell Signaling), ERK1/2 pT202/Y204 (D13.14.4E, Cell Signaling), Paxillin pY-118 (2541S, Cell Signaling), PAK1/2/3 (2604P, Cell Signaling), PAK1 pS144 (2606P, Cell Signaling), FACS antibodies; human CD44 (IM7, Biolegend, San Diego, CA, USA), CD24 (M1/69, Biolegend).

Surface plasmon resonance

Quantitative analysis of the EZH2–VAV interaction using VAV1$_{1-172}$ and mutant forms of EZH2$_{201-252}$ was performed using BIACORE 3000. A 4000 RU anti-GST surface was prepared on a standard CM5 sensor chip (GE Healthcare, Chicago, IL, USA) by amine-coupling anti-GST antibody (GST Capture Kit, GE Healthcare) on all four flow cells. Subsequent interaction assays were performed by capturing ~2700 RU of GST–VAV1$_{1-172}$ (equivalent GST on separate flow cell as control) using a buffer of 10 mM PBS, 137 mM NaCl, 2.7 mM KCl, pH 7.4 at 25 °C. A typical cycle of interaction comprises: (1) stabilization in running buffer, (2) capturing of ligand, (3) stabilization after ligand capture, (4) interaction with analytes, (5) dissociation of analytes and (6) regeneration of surface with 1:10 phosphoric acid. Several concentrations (32 nM/16.7 μM) of EZH2–HIS and its mutants were injected across control and GST–VAV1-captured surface for 2 min at a flow rate of 30 μl/min. The equilibrium response for each EZH2–HIS concentration was converted to surface ligand occupancy by dividing $R_{\max}$. These occupancy responses were plotted against the log concentration of EZH2–HIS as standard dose–response curves and a steady-state model was used to fit the points. The affinity constants were interpolated from 50% occupancy.

In vitro methyltransferase assay

Full-length wild-type EZH2 or EZH2 with the individual mutations were incubated with recombinant histone octamer (0.2 μg) using *S*-adenosyl-l-[methyl-^{3}H] methionine ([^{3}H]-SAM) or cold SAM as the methyl donor. The reaction was carried out in methylation buffer (50 mM Tris, pH 8.0) containing 0.5 mM DTT, 7.6 μM (15 μci) of SAM at 30 °C for 1 h. The reaction was stopped by addition of 2× SDS gel loading buffer followed by SDS–PAGE. The gel was either stained with Coomassie Blue Brilliant and enhanced by EN3HANCE (PerkinElmer Life Sciences, Boston, MA, USA) for X-ray film exposure or transferred to a PVDF membrane (Millipore) and probed with anti-H3K27me3 or anti-pan-methyl-lysine antibodies.

Immunofluorescence staining

Immunofluorescence staining was performed according to standard protocols. H16N2 cells stably expressing different forms of EZH2, as described, were plated on glass slides at a concentration of 3.0×10^{5} per well. Cells were starved of EGF for 3 days and then stimulated with EGF (30 ng/ml) for 12 h. They were then fixed with 2% paraformaldehyde for 30 min and permeabilized with 0.1% Triton X-100 for 2 min, washed and stained for F-actin with fluorescein isothiocyanate- or rhodamine red-conjugated or Alexa Fluor 647 Phalloidin (Molecular Probes/Thermo Fisher, Waltham, MA, USA). Slides were blocked with 10% normal donkey serum for 1 h, then stained with anti-Paxillin (05-417PC12-305, Millipore) or anti-GFP (ab290, Abcam) antibodies in PBS/bovine serum albumin (BSA) at 4 °C overnight and then incubated with anti-mouse Rhodamine secondary antibody or anti-rabbit FITC (Jackson ImmunoResearch, West Grove, PA, USA) antibody in PBS/BSA at room temperature for 1 h. Slides were then mounted with DAPI (Invitrogen, Carlsbad, CA, USA) containing mounting medium (Ibidi GmbH, Munich, Germany) and observed using a ×60 objective by immunofluorescence microscopy.

Live cell imaging for adhesion assembly and disassembly

Live cell imaging was performed using an inverted epifluorescent microscope Eclipse Ti microscope (Nikon, Shinagawa, Japan) at ×100 magnification. Images of live cells were recorded at a time-lapse interval of 2 min over a period of 1–2 h using an ORCA-Flash 4.0 camera (Hamatsu, Shizuoka, Japan) with the MetaMorph Imaging System 7.8 (Molecular Devices, Sunnyvale, CA, USA). Time-lapse images were reconstructed as image stacks (MetaMorph/Molecular Devices, Sunnyvale, CA, USA). The background and photobleaching-corrected integrated fluorescence intensities in individual adhesion based on mCherry-Paxillin or GFP-Talin1 were determined manually using the 'integrated density' measurement function of Image J software (NIH, Bethesda, MD, USA). Focal complexes and focal adhesions with a size between 0.2 and 19 μm^{2} were scored. Integrated fluorescence intensities were plotted against time. A linear trendline fitted to the data was used to identify the period of linear assembly or disassembly of the adhesions. The rate constants of assembly (k_a) and disassembly (k_d) were calculated using the equations: $k_a = -\frac{\ln(I/I_0)}{(t-t_0)}$ and $k_d = -\frac{\ln(I_0/I)}{(t_0-t)}$, where I is the intensity of the adhesion at a given time point and I_0 is the initial intensity of the adhesion. Rate constants were used to calculate half-life ($t_{1/2}$) values for adhesion assembly and disassembly using the equation: $t_{1/2} = \frac{\ln(2)}{k_a \text{or} k_d}$.

Anchorage-independent cell growth assay

Anchorage-independent growth of H16N2 cells stably expressing various forms of EZH2 was tested in 24-well culture plates. About 200 μl of F12 culture medium with 0.6% soft agar was first plated into each well of a 24-well plate. After the solidification of agar, each well received another 1 ml of 0.4% agar in culture medium containing 15 000 cells. After 25–30 days, colonies were fixed and stained with 0.1% crystal violet. The number of colonies from triplicate wells for each cell line was determined using Image J software (NIH).

Mammary tumor models

Inguinal mammary fat pads of 6-week-old female NOD-SCID mice or BALB/c mice were inoculated with 7×10^6 of MDA-MB-231 cells or 1×10^6 of EZH2 knockdown 4T1 cells expressing different forms of EZH2 variants. Tumor growth was monitored at the indicated time points by measuring tumor dimensions (length and width) using Vernier calipers or fluorescence intensity using IVIS Spectrum CT (PerkinElmer) 24 h after i.v. injection of 2-DG750 (10 nmoles/100 μl). To estimate the tumor volume measured by Vernier calipers, we assumed the tumor shape was a cylinder and calculated the volume of the cylinder by multiplying the ellipse area by the estimated depth (we took whichever was larger between width and length as depth). The actual depth and tumor volume cannot be measured in live animals using this method. At the end of the experimental period, mice were killed, tumors and other organs were resected, and either weighed and fixed with 10% paraformaldehyde for tissue sectioning or the fluorescence intensity was measured by IVIS Spectrum CT. All mice were bred and maintained under specific pathogen-free conditions at the animal facility of the School of Biological Sciences, Nanyang Technological University. All mouse protocols were conducted in accordance with the guidelines of the NTU Institutional Animal Care and Use Committee (IACUC).

RNA-seq

EZH2 knockdown H16N2 cells transduced with control (MIG) or retrovirus to express the indicated EZH2 variants were seeded in six-well plates for 48 h. RNA from these cells was isolated using the QIAshredder (Qiagen, Hilden, Germany) and RNeasy (Qiagen) kits. The total RNA quality and RIN value was confirmed with a 2100 Bioanalyzer (Agilent, Santa Clara, CA, USA) using RNA 6000 Nano chip (Agilent). Library preparation was done using the Illumina TruSeq Stranded messenger RNA LT Sample Prep Kit, by following the manufacturer's protocol. Each sample was linearized, denatured and loaded into two lanes of Single-Read flowcell using the Illumina cBOT. The cDNAs were attached to the flowcell surfaces and amplified to clusters and attached with sequencing primers. The flowcell was then loaded into the Illumina HiSeq2000 Sequencer with the Illumina HiSeq SBS Kit and run at 1×101 cycles, generating Single-Read 100 base-pair reads. The images were captured by the HiSeq Control Software (HCS, Illumina, San Diego, CA, USA), and the Real Time Analysis (RTA, Illumina, San Diego, CA, USA) software converted the images into Cycle Intensity Files (CIF) and, subsequently, Basecall (bcl) files. RNA-Seq data were mapped against the human genome version hg19 with TopHat2, using the GENCODE Release 19 version of gene annotations. Fragments per kilobase million values were extracted for the RNA-Seq analysis. Reads were counted using the R package GenomicAlignments (mode = 'Union', inter. feature = FALSE), only primary read alignments were retained. DEGs were identified using DESeq2. The DEGs for the four conditions (MIG, EZH2ΔNLS, EZH2H689A and EZH2–VAV/MT) were calculated in comparison to EZH2. If the log2-fold change of a gene was higher than 0 and its adjusted *P*-value was smaller than 0.05, the gene was highlighted as upregulated. If the log2-fold change of a gene was smaller than 0 and its adjusted *P*-value was smaller than 0.05, the gene was highlighted as downregulated. The heatmap was created by using ggplot2_1.0.0 (for detailed references, see Supplementary Experimental Procedures). Normalized fragments per kilobase million values of these significantly expressed genes were shown as a heatmap in Figure 6a. The data were normalized such that the sum of the expression estimates of each gene was 1 (relative expression) and the normalized fragments per kilobase million value from the EZH2 sample was subtracted from the other samples in order to show the EZH2 sample as the baseline. Functional ontology analysis of DEGs (more than 0.3 of log2-fold increase or decrease and $P < 0.05$ relative to results obtained in wild-type EZH2-expressing cells) in cytosolic EZH2-expressing cells were classified using the DAVID Bioinformatics Resources online functional annotation tool (http://david.abcc.ncifcrf.gov/summary.jsp), then grouped by functional categories (see corresponding Supplementary Table S1 source data file for Figure 6).

Real-time PCR

RNA was extracted from H16N2 cells, as above, and subsequently converted to cDNA using the SuperScript III First-Strand Synthesis Kit (Invitrogen) with random hexamers as primers. The cDNA abundance was analyzed by SYBR green real-time PCR with respective primers using the StepOnePlus Real-Time PCR System (Applied Biosystems, Foster City, CA, USA). GAPDH was used as a reference gene. Fold change was calculated using the formula$2^{-\Delta\Delta Ct}$, where ΔΔCt = ΔCt sample—ΔCt reference sample and ΔCt = Ct target gene—Ct reference gene. The following primer sequences were used for each gene:

STAT1: 5′-CAGCTTGACTCAAAATTCCTGGA-3′, 5′-TGAAGATTACGCTTGCTTTTCCT-3′
STAT2: 5′-CCAGCTTTACTCGCACAGC-3′, 5′-AGCCTTGGAATCATCACTCCC-3′
STAT3: 5′-ACCAGCAGTATAGCCGCTTC-3′, 5′-GCCACAATCCGGGCAATCT-3′
IRF1: 5-ATGCCCATCACTCGGATGC-3′, 5′-CCCTGCTTTGTATCGGCCTG-3′
c-Fos: 5′-GGGGCAAGGTGGAACAGTTAT-3′, 5′-CCGCTTGGAGTGTATCAGTCA-3′
MMP7: 5′-GAGTGAGCTACAGTGGGAACA-3′, 5′-CTATGACGCGGGAGTTTAACAT-3′
MMP13: 5′-TCCTGATGTGGGTGAATACAATG-3′, 5′-GCCATCGTGAAGTCTGGTAAAAT-3′
TMPRSS15: 5′-GCCAGTGGATCATACGTGTAAA-3′, 5′-GTGCCAGGATTAGTTTCCCAAAT-3′
IFI27: 5′-GTGGACGTTCGGGAGCTAC-3′, 5′-ACTGGCCGATTTGGCACAG-3′

CONFLICT OF INTEREST

The authors declare no conflict of interest.

ACKNOWLEDGEMENTS

We thank S Strömblad for critical reading, discussions and comments on the manuscript; Y Zhang (Harvard University) for the EZH2, SUZ12 and EED baculovirus expression vectors; we thank Y Or for providing BALB/c mice and technical support, LY Lu for advice on statistical analysis and A Sullivan from Obrizus Communications for editing the manuscript. This work was supported by the Singapore Agency for Science Technology and Research (A*STAR) through a Biomedical Research Council (BMRC) grant (10/1/22/19/666) to LN, Singapore Ministry of Education (MOE2009-T2-1-034 and MOE2013-T2-2-038) and Ministry of Health, National Medical Research Council (NMRC-CBRG/0057/201) to I-hS.

ACCESSION CODES

ArrayExpress website: http://www.ebi.ac.uk/arrayexpress/help/how_to_search.html#Login

AUTHOR CONTRIBUTIONS

NV identified EZH2-mediated Talin methylation sites, initiated the project and established essential collaborations; NV and JFW designed and conducted most of the experiments, including the *in vitro* methyltransferase assays, identification of the EZH2–VAV interaction mutant and performed experiments in mammary epithelial cells, breast cancer animal models and were also involved in the data interpretation and manuscript preparation; KPT and MSM did computational modeling and predicted residues critical for EZH2–VAV interaction; HHC and VCLL were involved in experiments using breast cancer animal models; EC and JG performed differential expression analysis of RNA-seq data; YHY and SGS performed the SPR analysis; AA and LN produced recombinant octamers and I-hS designed and interpreted the experiments and wrote the manuscript.

REFERENCES

1 Kleer CG, Cao Q, Varambally S, Shen R, Ota I, Tomlins SA *et al.* EZH2 is a marker of aggressive breast cancer and promotes neoplastic transformation of breast epithelial cells. *Proc Natl Acad Sci USA* 2003; **100**: 11606–11611.

2 Morin RD, Johnson NA, Severson TM, Mungall AJ, An J, Goya R *et al.* Somatic mutations altering EZH2 (Tyr641) in follicular and diffuse large B-cell lymphomas of germinal-center origin. *Nat Genet* 2010; **42**: 181–185.

3 Varambally S, Dhanasekaran SM, Zhou M, Barrette TR, Kumar-Sinha C, Sanda MG *et al.* The polycomb group protein EZH2 is involved in progression of prostate cancer. *Nature* 2002; **419**: 624–629.

4 Cao Q, Yu J, Dhanasekaran SM, Kim JH, Mani RS, Tomlins SA *et al.* Repression of E-cadherin by the polycomb group protein EZH2 in cancer. *Oncogene* 2008; **27**: 7274–7284.

5 Chang CJ, Yang JY, Xia W, Chen CT, Xie X, Chao CH *et al.* EZH2 promotes expansion of breast tumor initiating cells through activation of RAF1-beta-catenin signaling. *Cancer Cell* 2011; **19**: 86–100.

6 Ren G, Baritaki S, Marathe H, Feng J, Park S, Beach S *et al.* Polycomb protein EZH2 regulates tumor invasion via the transcriptional repression of the metastasis suppressor RKIP in breast and prostate cancer. *Cancer Res* 2012; **72**: 3091–3104.

7 Yoo KH, Hennighausen L. EZH2 methyltransferase and H3K27 methylation in breast cancer. *Int J Biol Sci* 2012; **8**: 59–65.

8 Vire E, Brenner C, Deplus R, Blanchon L, Fraga M, Didelot C *et al.* The Polycomb group protein EZH2 directly controls DNA methylation. *Nature* 2006; **439**: 871–874.

9 Lee ST, Li Z, Wu Z, Aau M, Guan P, Karuturi RK *et al.* Context-specific regulation of NF-kappaB target gene expression by EZH2 in breast cancers. *Mol Cell* 2011; **43**: 798–810.

10 Gonzalez ME, Moore HM, Li X, Toy KA, Huang W, Sabel MS *et al.* EZH2 expands breast stem cells through activation of NOTCH1 signaling. *Proc Natl Acad Sci USA* 2014; **111**: 3098–3103.

11 Xu K, Wu ZJ, Groner AC, He HH, Cai C, Lis RT *et al.* EZH2 oncogenic activity in castration-resistant prostate cancer cells is Polycomb-independent. *Science* 2012; **338**: 1465–1469.

12 Kim E, Kim M, Woo DH, Shin Y, Shin J, Chang N *et al.* Phosphorylation of EZH2 activates STAT3 signaling via STAT3 methylation and promotes tumorigenicity of glioblastoma stem-like cells. *Cancer Cell* 2013; **23**: 839–852.

13 Zhu P, Wang Y, Huang G, Ye B, Liu B, Wu J *et al.* lnc-beta-Catm elicits EZH2-dependent beta-catenin stabilization and sustains liver CSC self-renewal. *Nat Struct Mol Biol* 2016; **23**: 631–639.

14 He A, Shen X, Ma Q, Cao J, von Gise A, Zhou P *et al.* PRC2 directly methylates GATA4 and represses its transcriptional activity. *Genes Dev* 2012; **26**: 37–42.

15 Lee JM, Lee JS, Kim H, Kim K, Park H, Kim JY *et al.* EZH2 generates a methyl degron that is recognized by the DCAF1/DDB1/CUL4 E3 ubiquitin ligase complex. *Mol Cell* 2012; **48**: 572–586.

16 Hock H. A complex Polycomb issue: the two faces of EZH2 in cancer. *Genes Dev* 2012; **26**: 751–755.

17 Ntziachristos P, Tsirigos A, Van Vlierberghe P, Nedjic J, Trimarchi T, Flaherty MS *et al.* Genetic inactivation of the polycomb repressive complex 2 in T cell acute lymphoblastic leukemia. *Nat Med* 2012; **18**: 298–301.

18 Zhang J, Ding L, Holmfeldt L, Wu G, Heatley SL, Payne-Turner D *et al.* The genetic basis of early T-cell precursor acute lymphoblastic leukaemia. *Nature* 2012; **481**: 157–163.

19 Chou RH, Yu YL, Hung MC. The roles of EZH2 in cell lineage commitment. *Am J Transl Res* 2011; **3**: 243–250.

20 Ezhkova E, Pasolli HA, Parker JS, Stokes N, Su IH, Hannon G *et al.* Ezh2 orchestrates gene expression for the stepwise differentiation of tissue-specific stem cells. *Cell* 2009; **136**: 1122–1135.

21 Hobert O, Jallal B, Ullrich A. Interaction of Vav with ENX-1, a putative transcriptional regulator of homeobox gene expression. *Mol Cell Biol* 1996; **16**: 3066–3073.

22 Su IH, Dobenecker MW, Dickinson E, Oser M, Basavaraj A, Marqueron R *et al.* Polycomb group protein ezh2 controls actin polymerization and cell signaling. *Cell* 2005; **121**: 425–436.

23 Su IH, Tarakhovsky A. Lysine methylation and 'signaling memory'. *Curr Opin Immunol* 2006; **18**: 152–157.

24 Boddicker RL, Razidlo GL, Dasari S, Zeng Y, Hu G, Knudson RA *et al.* Integrated mate-pair and RNA sequencing identifies novel, targetable gene fusions in peripheral T-cell lymphoma. *Blood* 2016; **128**: 1234–1245.

25 Campbell JD, Alexandrov A, Kim J, Wala J, Berger AH, Pedamallu CS *et al.* Distinct patterns of somatic genome alterations in lung adenocarcinomas and squamous cell carcinomas. *Nat Genet* 2016; **48**: 607–616.

26 Chang KH, Sanchez-Aguilera A, Shen S, Sengupta A, Madhu MN, Ficker AM *et al.* Vav3 collaborates with p190-BCR-ABL in lymphoid progenitor leukemogenesis, proliferation, and survival. *Blood* 2012; **120**: 800–811.

27 Kataoka K, Nagata Y, Kitanaka A, Shiraishi Y, Shimamura T, Yasunaga J *et al.* Integrated molecular analysis of adult T cell leukemia/lymphoma. *Nat Genet* 2015; **47**: 1304–1315.

28 Menacho-Marquez M, Garcia-Escudero R, Ojeda V, Abad A, Delgado P, Costa C *et al.* The Rho exchange factors Vav2 and Vav3 favor skin tumor initiation and promotion by engaging extracellular signaling loops. *PLoS Biol* 2013; **11**: e1001615.

29 Citterio C, Menacho-Marquez M, Garcia-Escudero R, Larive RM, Barreiro O, Sanchez-Madrid F *et al.* The rho exchange factors vav2 and vav3 control a lung metastasis-specific transcriptional program in breast cancer cells. *Sci Signal* 2012; **5**: ra71.

30 Thalappilly S, Soubeyran P, Iovanna JL, Dusetti NJ. VAV2 regulates epidermal growth factor receptor endocytosis and degradation. *Oncogene* 2010; **29**: 2528–2539.

31 Aghazadeh B, Lowry WE, Huang XY, Rosen MK. Structural basis for relief of autoinhibition of the Dbl homology domain of proto-oncogene Vav by tyrosine phosphorylation. *Cell* 2000; **102**: 625–633.

32 Katzav S, Martin-Zanca D, Barbacid M. vav, a novel human oncogene derived from a locus ubiquitously expressed in hematopoietic cells. *EMBO J* 1989; **8**: 2283–2290.

33 Groysman M, Nagano M, Shaanan B, Katzav S. Mutagenic analysis of Vav reveals that an intact SH3 domain is required for transformation. *Oncogene* 1998; **17**: 1597–1606.

34 Hobert O, Sures I, Ciossek T, Fuchs M, Ullrich A. Isolation and developmental expression analysis of Enx-1, a novel mouse Polycomb group gene. *Mech Dev* 1996; **55**: 171–184.

35 Rudolph MG, Stanfield RL, Wilson IA. How TCRs bind MHCs, peptides, and coreceptors. *Annu Rev Immunol* 2006; **24**: 419–466.

36 Jiao L, Liu X. Structural basis of histone H3K27 trimethylation by an active polycomb repressive complex 2. *Science* 2015; **350**: aac4383.

37 Gunawan M, Venkatesan N, Loh JT, Wong JF, Berger H, Neo WH *et al.* The methyltransferase Ezh2 controls cell adhesion and migration through direct methylation of the extranuclear regulatory protein talin. *Nat Immunol* 2015; **16**: 505–516.

38 Harrington EA, Fanidi A, Evan GI. Oncogenes and cell death. *Curr Opin Genet Dev* 1994; **4**: 120–129.

39 Masuda H, Zhang D, Bartholomeusz C, Doihara H, Hortobagyi GN, Ueno NT. Role of Epidermal growth factor receptor in breast cancer. *Breast Cancer Res Treat* 2012; **136**: 331–345.

40 Huq MD, Tsai NP, Khan SA, Wei LN. Lysine trimethylation of retinoic acid receptor-alpha: a novel means to regulate receptor function. *Mol Cell Proteomics* 2007; **6**: 677–688.

41 Zhang Y, Yang X, Gui B, Xie G, Zhang D, Shang Y *et al.* Corepressor protein CDYL functions as a molecular bridge between polycomb repressor complex 2 and repressive chromatin mark trimethylated histone lysine 27. *J Biol Chem* 2011; **286**: 42414–42425.

42 Cao Q, Wang X, Zhao M, Yang R, Malik R, Qiao Y *et al.* The central role of EED in the orchestration of polycomb group complexes. *Nat Commun* 2014; **5**: 3127.

43 Pasini D, Bracken AP, Jensen MR, Denchi EL, Helin K. Suz12 is essential for mouse development and for EZH2 histone methyltransferase activity. *EMBO J* 2004; **23**: 4061–4071.

44 Lee TC, Ziff EB. Mxi1 is a repressor of the c-Myc promoter and reverses activation by USF. *J Biol Chem* 1999; **274**: 595–606.

45 Rodriguez JL, Sandoval J, Serviddio G, Sastre J, Morante M, Perrelli MG *et al.* Id2 leaves the chromatin of the E2F4-p130-controlled c-myc promoter during hepatocyte priming for liver regeneration. *Biochem J* 2006; **398**: 431–437.

46 Wierstra I, Alves J. The c-myc promoter: still MysterY and challenge. *Adv Cancer Res* 2008; **99**: 113–333.

47 Nicolaidou V, Wong MM, Redpath AN, Ersek A, Baban DF, Williams LM *et al.* Monocytes induce STAT3 activation in human mesenchymal stem cells to promote osteoblast formation. *PLoS ONE* 2012; **7**: e39871.

48 Yu H, Jove R. The STATs of cancer--new molecular targets come of age. *Nat Rev Cancer* 2004; **4**: 97–105.

49 Dasgupta M, Dermawan JK, Willard B, Stark GR. STAT3-driven transcription depends upon the dimethylation of K49 by EZH2. *Proc Natl Acad Sci USA* 2015; **112**: 3985–3990.

50 Yang J, Huang J, Dasgupta M, Sears N, Miyagi M, Wang B *et al.* Reversible methylation of promoter-bound STAT3 by histone-modifying enzymes. *Proc Natl Acad Sci USA* 2010; **107**: 21499–21504.

51 Chung J, Uchida E, Grammer TC, Blenis J. STAT3 serine phosphorylation by ERK-dependent and -independent pathways negatively modulates its tyrosine phosphorylation. *Mol Cell Biol* 1997; **17**: 6508–6516.

52 Normanno N, De Luca A, Bianco C, Strizzi L, Mancino M, Maiello MR *et al.* Epidermal growth factor receptor (EGFR) signaling in cancer. *Gene* 2006; **366**: 2–16.

53 Tanos B, Rodriguez-Boulan E. The epithelial polarity program: machineries involved and their hijacking by cancer. *Oncogene* 2008; **27**: 6939–6957.

54 Lock JG, Mamaghani MJ, Shafqat-Abbasi H, Gong X, Tyrcha J, Stromblad S. Plasticity in the macromolecular-scale causal networks of cell migration. *PLoS One* 2014; **9**: e90593.

55 Nagano M, Hoshino D, Koshikawa N, Akizawa T, Seiki M. Turnover of focal adhesions and cancer cell migration. *Int J Cell Biol* 2012; **2012**: 310616.

56 Jain N, Iyer KV, Kumar A, Shivashankar GV. Cell geometric constraints induce modular gene-expression patterns via redistribution of HDAC3 regulated by actomyosin contractility. *Proc Natl Acad Sci USA* 2013; **110**: 11349–11354.

57 Vergani L, Grattarola M, Nicolini C. Modifications of chromatin structure and gene expression following induced alterations of cellular shape. *Int J Biochem Cell Biol* 2004; **36**: 1447–1461.

58 Hsieh FC, Cheng G, Lin J. Evaluation of potential Stat3-regulated genes in human breast cancer. *Biochem Biophys Res Commun* 2005; **335**: 292–299.

59 Gialeli C, Theocharis AD, Karamanos NK. Roles of matrix metalloproteinases in cancer progression and their pharmacological targeting. *FEBS J* 2011; **278**: 16–27.

60 Rangel LB, Agarwal R, D'Souza T, Pizer ES, Alo PL, Lancaster WD *et al.* Tight junction proteins claudin-3 and claudin-4 are frequently overexpressed in ovarian cancer but not in ovarian cystadenomas. *Clin Cancer Res* 2003; **9**: 2567–2575.

61 Matsuguchi T, Inhorn RC, Carlesso N, Xu G, Druker B, Griffin JD. Tyrosine phosphorylation of p95Vav in myeloid cells is regulated by GM-CSF, IL-3 and steel factor and is constitutively increased by p210BCR/ABL. *EMBO J* 1995; **14**: 257–265.

62 Natsume A, Ito M, Katsushima K, Ohka F, Hatanaka A, Shinjo K *et al.* Chromatin regulator PRC2 is a key regulator of epigenetic plasticity in glioblastoma. *Cancer Res* 2013; **73**: 4559–4570.

63 Tan J, Yang X, Zhuang L, Jiang X, Chen W, Lee PL *et al.* Pharmacologic disruption of Polycomb-repressive complex 2-mediated gene repression selectively induces apoptosis in cancer cells. *Genes Dev* 2007; **21**: 1050–1063.

64 McCabe MT, Ott HM, Ganji G, Korenchuk S, Thompson C, Van Aller GS *et al.* EZH2 inhibition as a therapeutic strategy for lymphoma with EZH2-activating mutations. *Nature* 2012; **492**: 108–112.

65 Knutson SK, Wigle TJ, Warholic NM, Sneeringer CJ, Allain CJ, Klaus CR *et al.* A selective inhibitor of EZH2 blocks H3K27 methylation and kills mutant lymphoma cells. *Nat Chem Biol* 2012; **8**: 890–896.

66 Chen YT, Zhu F, Lin WR, Ying RB, Yang YP, Zeng LH. The novel EZH2 inhibitor, GSK126, suppresses cell migration and angiogenesis via down-regulating VEGF-A. *Cancer Chemother Pharmacol* 2016; **77**: 757–765.

67 Kim KH, Roberts CW. Targeting EZH2 in cancer. *Nat Med* 2016; **22**: 128–134.

68 Toh TB, Lim JJ, Chow EKH. Epigenetics in cancer stem cells. *Mol Cancer* 2017; **16**: 29.

69 Yu J, Yu J, Rhodes DR, Tomlins SA, Cao X, Chen G *et al.* A polycomb repression signature in metastatic prostate cancer predicts cancer outcome. *Cancer Res* 2007; **67**: 10657–10663.

70 Su IH, Basavaraj A, Krutchinsky AN, Hobert O, Ullrich A, Chait BT *et al.* Ezh2 controls B cell development through histone H3 methylation and Igh rearrangement. *Nat Immunol* 2003; **4**: 124–131.

71 Chen YH, Hung MC, Li LY. EZH2: a pivotal regulator in controlling cell differentiation. *Am J Transl Res* 2012; **4**: 364–375.

72 Juan AH, Kumar RM, Marx JG, Young RA, Sartorelli V. Mir-214-dependent regulation of the polycomb protein Ezh2 in skeletal muscle and embryonic stem cells. *Mol Cell* 2009; **36**: 61–74.

73 Kamminga LM, Bystrykh LV, de Boer A, Houwer S, Douma J, Weersing E *et al.* The Polycomb group gene Ezh2 prevents hematopoietic stem cell exhaustion. *Blood* 2006; **107**: 2170–2179.

74 Lee TI, Jenner RG, Boyer LA, Guenther MG, Levine SS, Kumar RM *et al.* Control of developmental regulators by Polycomb in human embryonic stem cells. *Cell* 2006; **125**: 301–313.

75 de Vries NA, Hulsman D, Akhtar W, de Jong J, Miles DC, Blom M *et al.* Prolonged Ezh2 depletion in glioblastoma causes a robust switch in cell fate resulting in tumor progression. *Cell Rep* 2015; **10**: 383–397.

76 Wassef M, Rodilla V, Teissandier A, Zeitouni B, Gruel N, Sadacca B *et al.* Impaired PRC2 activity promotes transcriptional instability and favors breast tumorigenesis. *Genes Dev* 2015; **29**: 2547–2562.

77 Zhao E, Maj T, Kryczek I, Li W, Wu K, Zhao L *et al.* Cancer mediates effector T cell dysfunction by targeting microRNAs and EZH2 via glycolysis restriction. *Nat Immunol* 2016; **17**: 95–103.

78 De Craene B, Berx G. Regulatory networks defining EMT during cancer initiation and progression. *Nat Rev Cancer* 2013; **13**: 97–110.

79 Herranz N, Pasini D, Diaz VM, Franci C, Gutierrez A, Dave N *et al.* Polycomb complex 2 is required for E-cadherin repression by the Snail1 transcription factor. *Mol Cell Biol* 2008; **28**: 4772–4781.

80 Sauvageau M, Sauvageau G. Polycomb group proteins: multi-faceted regulators of somatic stem cells and cancer. *Cell Stem Cell* 2010; **7**: 299–313.

81 Webb DJ, Donais K, Whitmore LA, Thomas SM, Turner CE, Parsons JT *et al.* FAK-Src signalling through paxillin, ERK and MLCK regulates adhesion disassembly. *Nat Cell Biol* 2004; **6**: 154–161.

Supplementary Information accompanies this paper on the *Oncogene* website (http://www.nature.com/onc)